J. Fluid Mech. (2022), *vol*. 951, A1, doi:10.1017/jfm.2022.823

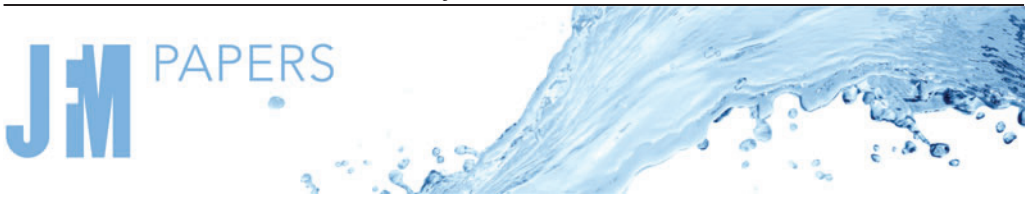

Impact of spanwise effective slope upon rough-wall turbulent channel flow

T.O. Jelly[1],†, A. Ramani[2], B. Nugroho[2], N. Hutchins[2] and A. Busse[3]

[1]Department of Engineering, University of Leicester, Leicester LE1 7RH, UK

[2]Department of Mechanical Engineering, University of Melbourne, Victoria 3010, Australia

[3]James Watt School of Engineering, University of Glasgow, G12 8QQ, UK

(Received 4 January 2022; revised 30 August 2022; accepted 23 September 2022)

Whereas streamwise effective slope (ES_x) is accepted as a key topographical parameter in the context of rough-wall turbulent flows, the significance of its spanwise counterpart (ES_y) remains largely unexplored. Here, the response of turbulent channel flow over irregular, three-dimensional rough walls with systematically varied values of ES_y is studied using direct numerical simulation. All simulations were performed at a fixed friction Reynolds number 395, corresponding to a viscous-scaled roughness height $k^+ \approx 65.8$ (where k is the mean peak-to-valley height). A surface generation algorithm is used to synthesise a set of ten irregular surfaces with specified ES_y for three different values of ES_x. All surfaces share a common mean peak-to-valley height and are near-Gaussian, which allows this study to focus on the impact of varying ES_y, since roughness amplitude, skewness and ES_x can be eliminated simultaneously as parameters. Based on an analysis of first- and second-order velocity statistics, as well as turbulence co-spectra and the fractional contribution of pressure and viscous drag, the study shows that ES_y can strongly affect the roughness drag penalty – particularly for low-ES_x surfaces. A secondary observation is that particular low-ES_y surfaces in this study can lead to diminished levels of outer-layer similarity in both mean flow and turbulence statistics, which is attributed to insufficient scale separation between the outer length scale and the in-plane spanwise roughness wavelength.

Key words: turbulence simulation

† Email address for correspondence: tj119@leicester.ac.uk

1. Introduction

Surface roughness is prevalent in many practical flows. Examples include flow through rough pipes (Allen *et al.* 2007), flow past bio-fouled ship hulls (Utama *et al.* 2021) and flow over vegetation canopies (Brunet 2020). It is well known that a hydrodynamically rough surface experiences an increased level of drag relative to a smooth surface at matched flow conditions (Moody 1944), and that practical surfaces often exhibit irregular roughness across a wide range of length scales, e.g. turbine-blade roughness (Barros & Christensen 2014), machined surfaces (Thakkar, Busse & Sandham 2016) and additively manufactured parts (Townsend *et al.* 2016). Yet predicting the drag penalty of irregular, multi-scale roughness remains an elusive goal and continues to be a focal point of research (Flack 2018; Chung *et al.* 2021).

In practice, the drag penalty due to surface roughness is described using a single parameter: the Nikuradse (1933) sand-grain roughness, k_s. However, k_s cannot be derived from any direct measure of roughness, e.g. using digital data obtained from a surface scan. Instead, an equivalent value of k_s must be assigned to a particular surface by exposing it to a range of known flow conditions and then relating measurements of the Hama (1954) roughness function $\Delta U^+ \equiv \Delta U/u_\tau$, or the skin-friction coefficient $C_f \equiv \tau_w/(\frac{1}{2}\rho U_b^2)$, to the Nikuradse (1933) sand-grain data. Here, ΔU^+ is the downward shift of the inner-scaled mean streamwise velocity profile in the logarithmic (log) layer, relative to the smooth-wall profile at matched flow conditions, and $u_\tau \equiv \sqrt{\tau_w/\rho}$ is the friction velocity, where τ_w is the wall shear stress, ρ is the density, and U_b is the streamwise bulk velocity. To express k_s in terms of some measure for the physical roughness height, say k, a scaling factor $C = k_s/k$ can be determined by collapsing the measured values of ΔU^+ onto Nikuradse's fully rough asymptote, $\Delta U^+_{FR}(k_s^+) = \kappa^{-1}\log k_s^+ + A - 8.5$, where subscript FR denotes fully rough conditions, κ is the von Kármán constant, $k_s^+ \equiv k_s u_\tau/\nu$ is the viscous-scaled sand-grain roughness, and A is the smooth-wall intercept. However, the scaling factor $C = k_s/k$ is surface-specific and must be determined for each type of roughness, e.g. virtual sandpaper roughness (Yuan & Piomelli 2014), egg-carton roughness (Chan *et al.* 2015), tube-worm roughness (Monty *et al.* 2016), grit-blasted roughness (Thakkar, Busse & Sandham 2018), irregular near-Gaussian roughness (Jelly & Busse 2019*b*), orange-peel roughness (Nugroho *et al.* 2021) or industrial grade sandpaper roughness (Berghout *et al.* 2021). Models that reliably predict k_s/k (or ΔU^+) based solely on key topographical parameters are therefore of great value.

Whilst the ultimate goal for roughness research is to produce a universal model that correlates key topographical parameters to k_s/k (or ΔU^+ for transitionally rough flows), a complete exploration of the parameter space that defines the 'roughness problem' is simply not feasible. To overcome this challenge, it is widely accepted that a minimal set of key topographical parameters must first be identified (Flack 2018; Chung *et al.* 2021), which can then be used to develop predictive models for k_s/k or ΔU^+. Eight predictive models for k_s/k and ΔU^+ proposed in past work are listed in table 1. Despite their variety, the models share three common topographical parameters. These include: (i) a measure of the physical roughness height, e.g. the mean absolute height S_a, the root-mean-square (r.m.s.) height S_q, or the mean peak-to-valley height $S_{z,5\times5}$; (ii) the skewness of the height distribution Ssk; and (iii) the streamwise effective slope ES_x. The latter quantity is defined as $ES_x = A^{-1}\int_A |\partial h(x,y)/\partial x|\,\mathrm{d}A$ (where $h(x,y)$ is the roughness height distribution, and A is the planform area of the surface), and is related to frontal solidity through the formula $\lambda_x \equiv \frac{1}{2}ES_x$ (see MacDonald *et al.* (2016) for details). Although models based

Reference	Roughness	Empirical model for k_s/k or ΔU^+
Townsin (1991)	Ship hull	$\Delta U^+ = \kappa^{-1} \ln\left[m_0\sqrt{m_4/m_2}\left(\frac{u_\tau}{\nu}\right)+1\right]$
Van Rij, Belnap & Ligrani (2002)	Turbine blade	$\frac{k_s}{k} = \begin{cases} 1.583\times10^{-5}\Lambda_s, & \Lambda_s \le 7.842, \\ 1.802\Lambda_s^{0.03038}, & 7.842 \le \Lambda_s \le 28.12, \\ 1.583\times10^{-5}\Lambda_s, & 28.12 \le \Lambda_s, \end{cases}$ where k is the roughness height
Bons (2005)	Turbine blade	$\frac{k_s}{k} = a\alpha_{rms}^2 + b\alpha_{rms}$, where k is the average roughness height
Chan *et al.* (2015)	Egg-carton	$\Delta U^+ = f(k^+, ES_x) = a\log k^+ + b\log ES_x + c$, where k^+ is the sinusoidal semi-amplitude
Flack *et al.* (2016)	Irregular	$\frac{k_s}{k} = f(S_q, Ssk) = aS_q(1+Ssk)^b$, where k is S_q^+
Thakkar *et al.* (2016)	Surface scans	$\Delta U^+ = a\ln\left(\frac{S_f}{S}\right)\left[1+0.067\ln\left(\frac{L_{x,cor}}{k}\right)\right]+b$, where k is $S_{z,5\times5}$
Forooghi *et al.* (2017)	Irregular	$\frac{k_s}{k} = f(Ssk)\,g(ES_x)$, where k is S_q and where $f = (aSsk^2 + bSsk + c)$, $g = d(1-\exp[-eES_x])$
De Marchis *et al.* (2020)	Irregular	$\Delta U^+ = \kappa^{-1}\ln(ES_x k^+) + B$, where k^+ is either S_a^+ or S_q^+

Table 1. Predictive models for k_s/k and ΔU^+ based on topographical parameters, including: generalised Sigal–Danberg parameter $\Lambda_s = (S/S_f)(S_f/S_s)^{-1.6}$ (where S is the planform area of the corresponding smooth surface, S_f is the total projected frontal area of all the roughness elements, and S_s is the total area of all roughness elements wetted by the flow S); nth spectral moment $m_n = \int_0^\infty \kappa^n E_{hh}\,\mathrm{d}\kappa$ (where E_{hh} is the spectrum of surface elevation, and κ is an in-plane wavenumber); r.m.s. forward-facing surface angle $\alpha_{rms} = \sqrt{n_f^{-1}\sum_{j=1}^{n_f}\alpha_j^2}$ (where n_f is the total number of forward-facing roughness elements, the local forward-facing surface angle is $\alpha_j = \tan^{-1}(\Delta s^{-1}[h_{j+1}-h_j])$, and Δs is the streamwise spacing of the roughness elements); mean absolute roughness height $S_a = A^{-1}\iint|h(x,y)|\,\mathrm{d}A$; r.m.s. roughness height $S_q = \sqrt{A^{-1}\iint h(x,y)^2\,\mathrm{d}A}$; skewness $Ssk = A^{-1}S_q^{-3}\iint h(x,y)^3\,\mathrm{d}A$; kurtosis $Sku = A^{-1}S_q^{-4}\iint h(x,y)^4\,\mathrm{d}A$; streamwise effective slope $ES_x = A^{-1}\int_A|\partial h(x,y)/\partial x|\,\mathrm{d}A$; and streamwise correlation length based on a 0.2 cutoff criterion, $L_{x,cor}$. Note that A is the planform area of the height map $h(x,y)$.

on parameters (i)–(iii) have shown promise in predicting the roughness drag penalty (Forooghi *et al.* 2017), a truly universal correlation will likely depend on additional topographical parameters related to other surface properties such as directionality or anisotropy.

Whilst the drag behaviours of highly directional two-dimensional surfaces have been studied extensively, e.g. streamwise-aligned riblets (Gatti *et al.* 2020; Modesti *et al.* 2021), spanwise-aligned bars (Volino, Schultz & Flack 2009; Krogstad & Efros 2012) and spanwise-alternating rough-to-smooth surfaces (Bakhuis *et al.* 2020; Wangsawijaya *et al.* 2020), systematic studies of surface anisotropy in the context of irregular, three-dimensional roughness remain scarce. One exception to this trend is the work by Busse & Jelly (2020), which demonstrated that irregular roughness with spanwise-elongated features induces an over 200 % increase in ΔU^+, relative to roughness

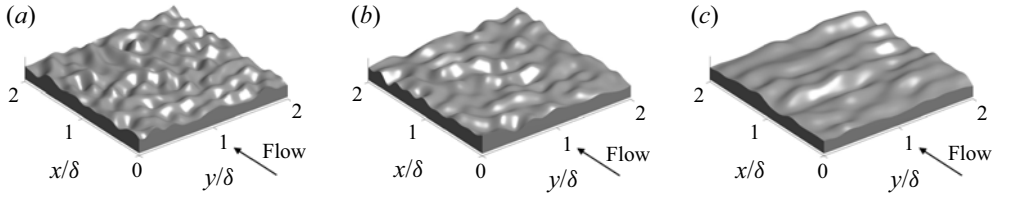

Figure 1. Irregular surface roughness with identical mean peak-to-valley height $S_{z,5\times5}/\delta = 1/6$, skewness $Ssk \approx 0$ and $ES_x \approx 0.35$, but differing ES_y. (*a*) Isotropic surface with $ES_y/ES_x = 1$. (*b*) Spanwise-elongated roughness with $ES_y/ES_x \approx 0.63$. (*c*) Spanwise-elongated roughness with $ES_y/ES_x \approx 0.29$. Each surface is shown on a $(2 \times 2)/\delta$ tile, where δ is the mean channel half-height.

with streamwise-elongated features in fully developed turbulent channel flow. In that work, the level of surface anisotropy was quantified using the surface anisotropy ratio (SAR) parameter, which was defined as SAR $\equiv L_{x,cor}/L_{y,cor}$, where $L_{x,cor}$ and $L_{y,cor}$ are the streamwise and spanwise correlation lengths based on a 0.2 cutoff criterion (see Thakkar *et al.* (2016) for details). Yet the sensitivity of wall drag with respect to the SAR parameter or other measures of surface anisotropy cannot be predicted using any combination of the topographical parameters included in table 1. This shortcoming is illustrated by the three roughness topographies shown in figure 1, which, based on their mean peak-to-valley height, skewness and streamwise effective slope, are identical in the statistical sense – despite showing obvious differences along the spanwise (y) direction. Hence further consideration of directional topographical parameters is required to predict the drag penalty of anisotropic surface roughness.

As a first step, spanwise effective slope ES_y can be considered, which, in analogy to ES_x, is defined as the mean absolute spanwise slope of the height distribution, $ES_y \equiv A^{-1}\int_A |\partial h(x,y)/\partial y|\,\mathrm{d}A$, and is related to 'lateral' solidity through the formula $\Lambda_y \equiv \frac{1}{2}ES_y$. The degree of surface anisotropy can then be inferred from the ratio of spanwise effective slope to streamwise effective slope, i.e. surfaces with $ES_y/ES_x = 1$ are isotropic (figure 1*a*), surfaces with $ES_y/ES_x < 1$ are spanwise-elongated (figures 1*b*,*c*), and surfaces with $ES_y/ES_x > 1$ are streamwise-elongated. The limiting cases are streamwise homogeneous roughness with $ES_x = 0$ and $ES_y > 0$, i.e. two-dimensional riblet-like surfaces with $ES_y/ES_x \to \infty$, and spanwise homogeneous roughness with $ES_x > 0$ and $ES_y = 0$, i.e. two-dimensional spanwise bar-like surfaces with $ES_y/ES_x \to 0$.

Whilst systematic studies of irregular anisotropic roughness ($ES_y/ES_x \neq 1$) remain scarce, the drag penalty of isotropic surface roughness ($ES_y/ES_x = 1$) has been studied for various regular (Bhaganagar, Kim & Coleman 2004; Coceal *et al.* 2006; Chan *et al.* 2015; Seddighi *et al.* 2015; Ma *et al.* 2020) and irregular (De Marchis *et al.* 2020; Flack, Schultz & Barros 2020; Ma, Alamé & Mahesh 2021; Nugroho *et al.* 2021; Portela, Busse & Sandham 2021) topographies. The current lack of studies on turbulent flow over surface roughness with systematically varied ES_x and ES_y is conveyed in figure 2, where data points from the present study and past work are plotted on the ES_x–ES_y plane. Relative to the combinations of ES_x and ES_y considered in the present study (shown as filled black circles in figure 2), most past data appear scattered, and few systematic patterns can be discerned. An exception to this trend is the past work of Busse & Jelly (2020), although, as was mentioned previously, that study focused on varying the SAR parameter systematically, and did not change ES_x or ES_y independently (see filled green circles in figure 2). Also, whilst practical roughness often shows appreciable levels of anisotropy

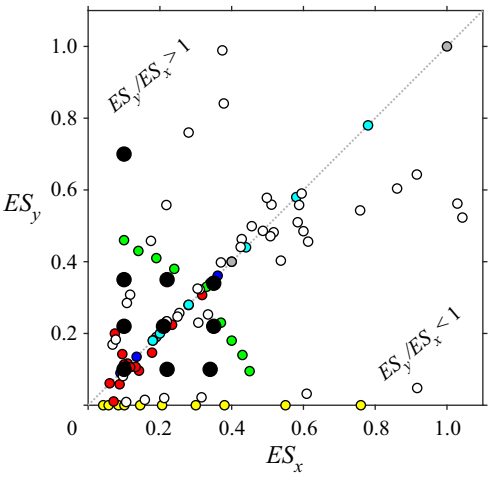

Figure 2. Combinations of ES_x and ES_y considered in the present study (black circles) and past work by: Napoli, Armenio & De Marchis (2008), yellow circles; Schultz & Flack (2009), grey circles; Chan *et al.* (2015), blue circles; Thakkar *et al.* (2016), red circles; Forooghi, Stripf & Frohnapfel (2018*a*), cyan circles; Busse & Jelly (2020), green circles; and Jouybari *et al.* (2021), white circles. The diagonal grey dotted line demarcates isotropic roughness $ES_y/ES_x = 1$.

(e.g. see surface scan data of Thakkar *et al.* (2016); filled red circles in figure 2), the values of ES_x and ES_y cannot be specified *a priori*, which complicates the analysis of results. Combined with the empirical models listed in table 1 and the data points plotted in figure 2, these past studies draw further attention to the lack of available data regarding the impact of ES_y upon rough-wall turbulent flows.

To determine whether or not ES_y should be considered an important topographical parameter, the present investigation takes a 'slice' through a region of the roughness parameter space that has not hitherto been explored. This is achieved by synthesising a set of ten irregular height maps with specified values of ES_y (whilst holding roughness amplitude, skewness and streamwise effective slope nearly constant), and then performing direct numerical simulations (DNS) of a rough-walled turbulent channel at friction Reynolds number 395 for each surface, corresponding to roughness Reynolds number $k^+ \approx 65.8$ (where k is the mean peak-to-valley height). The sensitivity of key hydrodynamic parameters, such as the Hama roughness function, and associated physical mechanisms, such as the relative contributions of pressure and viscous drag, are then quantified with respect to systematic variations in ES_y for a fixed value of k^+. Some observations regarding the levels of outer-layer similarity (or lack thereof) above particular low-ES_y surfaces are also discussed. The numerical aspects of this study are described in § 2. Results are presented in § 3. Finally, in § 4, the conclusions of this work are given.

2. Numerical aspects

This section describes the numerical aspects of this work and is divided into three parts. First, a description of the surface synthesis procedure is given. Second, the embedded boundary DNS algorithm used to simulate rough-wall turbulent channel flow is summarised, and key simulation parameters are provided. Finally, the statistical averaging procedure is described.

2.1. *Surface synthesis procedure*

Irregular three-dimensional surfaces with doubly periodic boundaries were generated by taking linear combinations of Gaussian random number matrices using a weighted moving average process based on past work by Patir (1978). Numerical details of the surface synthesis procedure are provided in Appendix A and/or in the past work of Jelly & Busse (2018, 2019*a*). The height distribution of each surface is near-Gaussian, i.e. zero mean, negligible skewness ($Ssk \approx 0$), and kurtosis equal to 3 ($Sku \approx 3$). The values of ES_x and ES_y for each surface were specified by varying the cutoff length of an exponential autocorrelation function in the streamwise (x_1) and spanwise (x_2) directions, and the cutoff wavenumber of a two-dimensional low-pass Fourier filter (Busse, Lützner & Sandham 2015). The filtered height maps were scaled to a common mean peak-to-valley height $S_{z,5\times5}/\delta = 1/6$, where δ is the channel half-height. Following Thakkar *et al.* (2016), the mean-peak-to-valley height was calculated by subdividing each height map into 5×5 tiles and then taking the average of the maximum peak-to-valley-heights of the different tiles. Thakkar *et al.* (2018) showed for an irregular, multi-scale rough surface resembling Nikuradse's sand-grain roughness that ΔU^+ becomes independent of $S_{z,5\times5}/\delta$ for fixed $S^+_{z,5\times5}$ when $S_{z,5\times5}/\delta \leq 1/6$; this criterion is met for all surfaces included in the present study.

Whilst all surfaces investigated here share a common mean peak-to-valley height, their mean absolute height (S_a) and r.m.s. roughness height (S_q) show some variation (see second and third columns in table 2). In particular, S_a varies by up to 26 % for Group A surfaces (see below), which could potentially mask the sensitivity of ΔU^+ with respect to ES_y. The impact of variations in S_a upon ΔU^+ can be estimated by recasting Nikuradse's fully rough asymptote as $\Delta U^+_{FR} = \kappa^{-1}\log(CS_a) + A - 8.5$, where $C = k_s/S_a$ is a surface-specific scaling factor. Multiplying S_a by a factor 1.26 would therefore change the Hama roughness function by approximately 0.6 wall units. As will be shown later, this variation is a factor of four smaller than the observed range of ΔU^+ for Group A surfaces. As a result, variations in S_a are herein considered to have a negligible effect on ΔU^+, relative to the impact of varying ES_y.

The ten roughness topographies investigated here are shown in figure 3. Each surface is named using the identification code

$$\underbrace{010}_{ES_x}\_\underbrace{035}_{ES_y}, \tag{2.1}$$

where the first three digits represent the value of the streamwise effective slope, e.g. $ES_x = 0.10$, and the last three three digits represent the value of the of the spanwise effective slope, e.g. $ES_y = 0.35$. Decimal points have been omitted for brevity. The ten surfaces were sorted into three groups according to their ES_x value. Group A contains four height maps, with $ES_x = 0.10$ and $ES_y = \{0.70, 0.35, 0.22, 0.10\}$. Group B contains three height maps, with $ES_x \approx 0.22$ and $ES_y = \{0.35, 0.22, 0.10\}$. Group C contains three height maps, with $ES_x \approx 0.35$ and $ES_y = \{0.35, 0.22, 0.10\}$. Further, according to the classification of Chung *et al.* (2021), Group A surfaces lie on the cusp of the sparse regime ($ES_x \lesssim 0.10$), Group C surfaces fall within the dense regime ($ES_x \gtrsim 0.30$), and Group B surfaces fall within an intermediate regime ($0.10 \lesssim ES_x \lesssim 0.30$). The present study therefore focuses mainly on the sparse and intermediate regimes. This choice was motivated by the surface scan data obtained by Thakkar *et al.* (2016) (filled red circles in figure 2), which shows that many practical surfaces satisfy the criterion $ES_x \lesssim 0.30$.

	ID code	$\frac{S_a}{\delta}$	$\frac{S_q}{\delta}$	Ssk	Sku	$\frac{S_{z,5\times5}}{\delta}$	$\frac{h_{max}}{\delta}$	ES_x	ES_y	$\frac{ES_y}{ES_x}$	$\frac{\bar{\lambda}_x}{\delta}$	$\frac{\bar{\lambda}_y}{\delta}$	$\frac{\bar{\lambda}_y}{\bar{\lambda}_x}$
A	010_070	0.025	0.033	0.00	2.93	0.167	0.120	0.10	0.70	7.00	2.86	0.24	0.08
	010_035	0.028	0.035	−0.01	2.99	0.167	0.109	0.10	0.35	3.50	2.34	0.50	0.21
	010_022	0.031	0.039	−0.05	3.03	0.167	0.128	0.10	0.22	2.20	2.14	0.86	0.40
	010_010	0.034	0.042	−0.06	2.97	0.167	0.121	0.10	0.10	1.00	1.96	1.76	0.90
B	022_035	0.023	0.029	0.01	3.01	0.167	0.119	0.22	0.35	1.59	0.82	0.43	0.52
	022_022	0.026	0.033	0.00	2.99	0.167	0.143	0.21	0.22	1.05	1.00	0.86	1.00
	022_010	0.027	0.033	0.01	2.90	0.167	0.109	0.22	0.10	0.45	0.80	1.79	2.24
C	035_035	0.022	0.028	0.01	3.00	0.167	0.102	0.34	0.34	1.00	0.46	0.44	0.96
	035_022	0.023	0.028	0.01	2.98	0.167	0.100	0.34	0.22	0.65	0.46	0.73	1.59
	035_010	0.025	0.031	−0.02	2.94	0.167	0.104	0.35	0.10	0.29	0.48	2.00	4.17

Table 2. Surface statistics, including: mean absolute height S_a; r.m.s. height S_q; skewness Ssk; kurtosis Sku; mean peak-to-valley height $S_{z,5\times5}$; height of the highest crest h_{max}; streamwise effective slope ES_x; spanwise effective slope ES_y; ratio of spanwise to streamwise effective slope ES_y/ES_x; ratio of mean streamwise in-plane wavelength to channel half-height $\bar{\lambda}_x/\delta$; ratio of mean spanwise in-plane wavelength to channel half-height $\bar{\lambda}_y/\delta$; and ratio of mean spanwise and streamwise in-plane wavelengths $\bar{\lambda}_y/\bar{\lambda}_x$.

To assign a particular spanwise length scale to each value of ES_y, the mean spanwise wavelength $\bar{\lambda}_y$ was obtained from the ratio of spectral moments (Townsin 2003), defined here as $\bar{\lambda}_y/(2\pi) \equiv m_0/m_1$, where the nth spectral moment is given by $m_n = \int_0^\infty \kappa_y^n E_{hh}\,\mathrm{d}\kappa_y$, with $\kappa_y E_{hh}$ the premultiplied spanwise spectra of the height distribution, and κ_y the in-plane spanwise wavenumber (see Chung *et al.* (2021) for details). The ratio $\bar{\lambda}_y/\delta$ is plotted against its streamwise counterpart $\bar{\lambda}_x/\delta$ for each surface in figure 4, spanning the ranges $0.5 \lesssim \bar{\lambda}_x/\delta \lesssim 3.0$ and $0.25 \lesssim \bar{\lambda}_y/\delta \lesssim 2.0$. For three out of the ten surfaces considered here, namely, 010_010, 022_010 and 035_010, the mean spanwise wavelength exceeds the outer length scale, i.e. $\bar{\lambda}_y/\delta > 1$. As will be shown later, insufficient scale separation between $\bar{\lambda}_y$ and δ can lead to atypical behaviour in both mean flow and turbulence statistics. The ratios $\bar{\lambda}_x/\delta$ and $\bar{\lambda}_y/\delta$ are listed in table 2 along with other key topographical parameters.

2.2. *Direct numerical simulations of rough-wall turbulent channel flow*

For each surface listed in table 2, DNS of incompressible fully developed turbulent channel flow with roughness on both the upper and lower walls were performed using the iterative embedded boundary algorithm of Busse *et al.* (2015), which has been employed in past works related to the present study, e.g. Thakkar *et al.* (2016, 2018), Jelly & Busse (2018, 2019*b*), Busse & Jelly (2020) and Portela *et al.* (2021). Second-order central differences are used for the discretisation of spatial derivatives. Time advancement is achieved using a second-order accurate Adams–Bashforth scheme. An iterative variant of the Yang & Balaras (2006) embedded boundary algorithm is used to resolve the rough walls. The velocity components in the streamwise (x_1 or x), spanwise (x_2 or y) and wall-normal (x_3 or z) directions are u_1, u_2 and u_3, respectively, and p is the fluctuating hydrodynamic pressure. The flow is driven by a constant (negative) streamwise pressure gradient Π, which defines the mean friction velocity as $u_\tau = \sqrt{(-\delta/\rho)\Pi}$. The friction Reynolds number

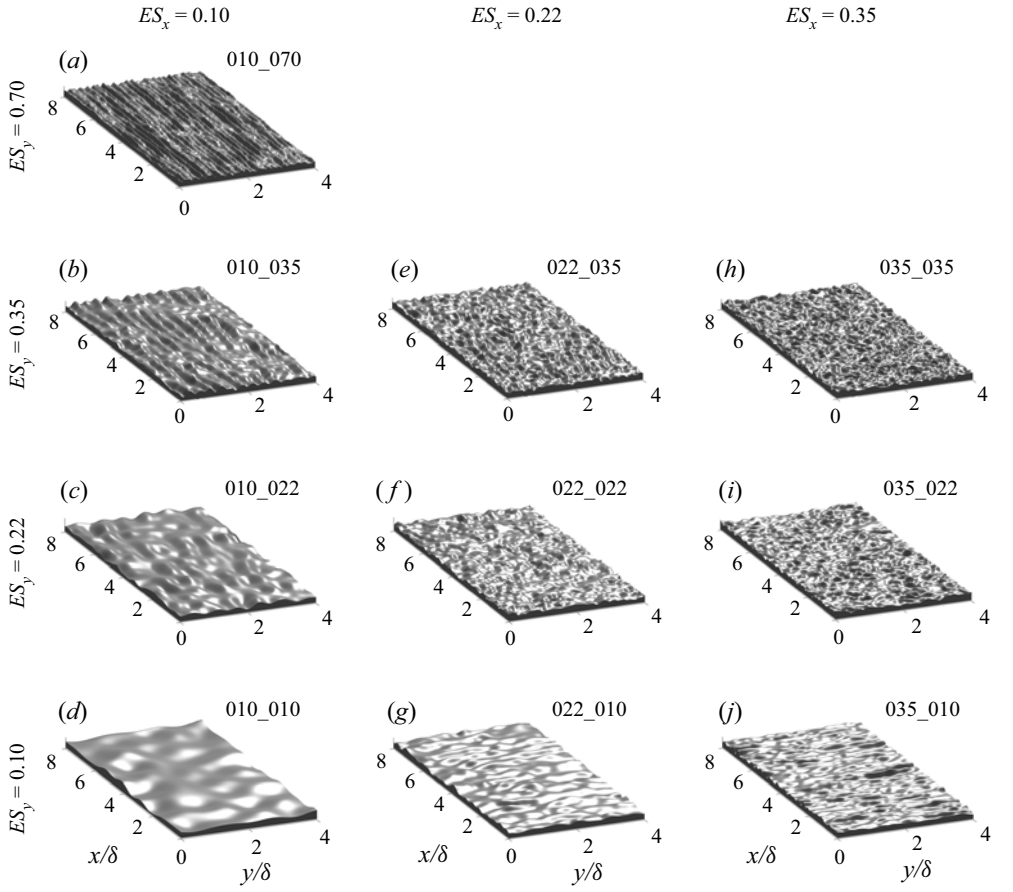

Figure 3. Surface topographies under consideration in this study. Streamwise effective slope (ES_x) remains constant in each column, whereas spanwise effective slope (ES_y) remains constant along each row. Group A surfaces: (*a*) 010_070, (*b*) 010_035, (*c*) 010_022, and (*d*) 010_010. Group B surfaces: (*e*) 022_035, (*f*) 022_022,and (*g*) 022_010. Group C surfaces: (*h*) 035_035, (*i*) 035_022, and (*j*) 035_010. The spanwise domain width for surfaces 010_010, 022_010 and 035_010 has been truncated by a distance 2δ for visualisation purposes.

is defined here as $Re_\tau \equiv u_\tau \delta/\nu$, where δ is the mean channel half-height, and ν is the kinematic viscosity. All simulations reported here were conducted at friction Reynolds number 395. For cases with $ES_y > 0.10$, a spanwise domain size $L_2/\delta = 4.0$ was specified. For the three cases with $ES_y = 0.10$, the spanwise domain size was increased by 50 % to $L_2/\delta = 6.0$ to ensure that the topographical features decorrelate within the spanwise extent of the domain. Inner-scaled quantities are marked by superscript +, e.g. time $t^+ = tu_\tau^2/\nu$, space $x_i^+ = x_i u_\tau/\nu$, and velocity $u_i^+ = u_i/u_\tau$. The key simulation parameters used throughout this study are consistent with the recommendations of Busse *et al.* (2015) and are listed in table 3.

For each simulation, data were accumulated for a minimum of $Tu_\tau/\delta = 40$ non-dimensional time units after the initial transient. In addition to collecting time-averaged data, instantaneous three-dimensional snapshots were also collected for further post-processing and analysis. Approximately 800 snapshots separated by twenty viscous-scaled time units, i.e. $\Delta t^+ \equiv \Delta t u_\tau^2/\nu \approx 20$, were obtained for each case listed

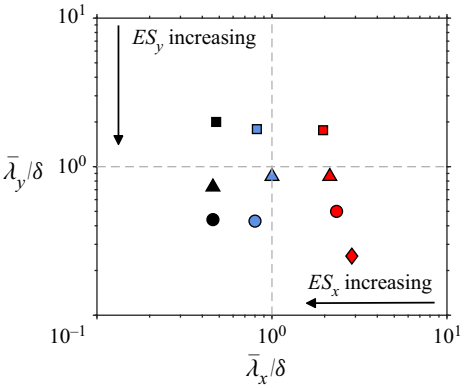

Figure 4. Ratio of mean in-plane spanwise wavelength and outer length scale of the flow, $\bar{\lambda}_y/\delta$, plotted against its streamwise counterpart $\bar{\lambda}_x/\delta$ for the ten surfaces under investigation in the present study. Symbol types and colours are given in table 3.

	ID code	$\frac{L_1}{\delta}$	$\frac{L_2}{\delta}$	$\frac{L_3}{\delta}$	N_1	N_2	N_3	Δx_1^+	Δx_2^+	$\Delta x_{3,min}^+$	$\Delta x_{3,max}^+$	Line	Symbol
A	010_070	8.0	4.0	2.0	640	720	576	4.94	2.19	0.67	4.66	- · -	♦
	010_035	8.0	4.0	2.0	640	320	576	4.94	4.94	0.67	4.66	——	●
	010_022	8.0	4.0	2.0	640	320	576	4.94	4.94	0.67	4.48	- - -	▲
	010_010	8.0	6.0	2.0	640	480	600	4.94	4.94	0.67	4.96	. . . .	■
B	022_035	8.0	4.0	2.0	640	320	576	4.94	4.94	0.67	4.48	——	●
	022_022	8.0	4.0	2.0	640	320	576	4.94	4.94	0.67	4.48	- - -	▲
	022_010	8.0	6.0	2.0	640	480	576	4.94	4.94	0.67	4.39	. . . .	■
C	035_035	8.0	4.0	2.0	640	320	576	4.94	4.94	0.67	4.95	——	●
	035_022	8.0	4.0	2.0	640	320	576	4.94	4.94	0.67	4.39	- - -	▲
	035_010	8.0	6.0	2.0	640	480	576	4.94	4.94	0.67	4.58	. . . .	■
	Smooth	8.0	4.0	2.0	480	240	320	6.58	6.58	0.17	4.26	——	

Table 3. Simulation parameters, including: domain sizes in the streamwise (L_1) and spanwise (L_2) directions; mean channel height L_3; numbers of points in the streamwise (N_1), spanwise (N_2) and wall-normal (N_3) directions; and viscous-scaled grid spacings, including streamwise (Δx_1^+), spanwise (Δx_2^+), minimum wall-normal ($\Delta x_{3,\min}^+$) and maximum wall-normal ($\Delta x_{3,\max}^+$) values. The line and symbol types for each case are also listed for reference.

in table 3. Reference smooth-wall data were also accumulated at matched flow conditions for comparison.

2.3. *Double-averaging methodology*

Statistical quantities were computed using a time-then-space averaging procedure, more commonly known as double-averaging (Raupach & Shaw 1982; Nikora *et al.* 2007). An instantaneous field variable, say $a(\boldsymbol{x}, t)$, can be double-averaged (DA) by applying first the time-averaging operator,

$$\bar{a}(\boldsymbol{x}) \equiv \lim_{T\to\infty} \frac{1}{T} \int_{t_0}^{t_0+T} a(\boldsymbol{x}, t)\, \mathrm{d}t, \tag{2.2}$$

and then the spatial-averaging operator,

$$\langle \bar{a} \rangle (x_3) \equiv \frac{1}{\phi(x_3)} \frac{1}{A} \iint_A \bar{a}(\boldsymbol{x}) \, \mathrm{d}x_1 \, \mathrm{d}x_2. \tag{2.3}$$

In (2.3), the void fraction function $\phi \equiv A_f(x_3)/A$ represents the ratio of the fluid-occupied area to the total area of the wall-parallel plane, $A = L_1 L_2$. Instantaneous field variables are set equal to zero in solid-occupied regions, i.e. $a(\boldsymbol{x}, t) = 0$. Averaging the flow in this way ensures that only fluid-occupied points contribute towards DA statistics beneath the roughness crests. The DA quantities reported herein therefore correspond to an intrinsic average (Gray & Lee 1977).

Considering (2.2) and (2.3), instantaneous field variables are decomposed as

$$a(\boldsymbol{x}, t) = \underbrace{\langle \bar{a} \rangle (x_3) + \tilde{a}(\boldsymbol{x})}_{\bar{a}(\boldsymbol{x})} + a'(\boldsymbol{x}, t), \tag{2.4}$$

where the dispersive component is defined as $\tilde{a}(\boldsymbol{x}) \equiv \bar{a}(\boldsymbol{x}) - \langle \bar{a} \rangle (x_3)$, and the turbulent component is defined as $a'(\boldsymbol{x}, t) \equiv a(\boldsymbol{x}, t) - [\langle \bar{a} \rangle (x_3) + \tilde{a}(\boldsymbol{x})]$. Using the triple decomposition (2.4), the local Reynolds stress tensor can be defined as

$$\boldsymbol{R}_{ij}(\boldsymbol{x}) \equiv \overline{(u_i - \bar{u}_i)(u_j - \bar{u}_j)} = \overline{u_i' u_j'}. \tag{2.5}$$

The spatial average of the local Reynolds stress tensor 2.5 is defined here as

$$\langle \boldsymbol{R}_{ij} \rangle (x_3) \equiv \langle \overline{u_i' u_j'} \rangle. \tag{2.6}$$

Finally, the dispersive stress tensor is defined here as

$$\boldsymbol{D}_{ij}(x_3) \equiv \big\langle (\bar{u}_i - \langle \bar{u}_i \rangle)(\bar{u}_j - \langle \bar{u}_j \rangle) \big\rangle = \langle \tilde{u}_i \tilde{u}_j \rangle. \tag{2.7}$$

3. Results

This section contains the key results of this study and is divided into four parts. First, the impact of ES_y upon the Hama roughness function is examined. Second, the effect of varying ES_y upon the fractional contribution of pressure and viscous drag to the total drag is examined. Third, the influence of ES_y upon first-order velocity statistics is discussed. Finally, the impact of ES_y upon second-order velocity statistics and turbulence co-spectra is discussed.

3.1. *Impact of spanwise effective slope upon the Hama roughness function*

Surface roughness induces a downward shift in the log-law velocity profile, relative to the smooth-wall profile at matched flow conditions, commonly referred to as the Hama (1954) roughness function, ΔU^+. Strictly speaking, ΔU^+ is an additive constant, which assumes that the inner-scale streamwise mean velocity difference between the smooth and rough walls – defined here as $\delta U^+(x_3^+) \equiv \langle u_1^+ \rangle_s(x_3^+) - \langle u_1^+ \rangle_r(x_3^+)$ – is uniform in the log region. Profiles of δU^+ normalised by the mean friction velocity are plotted against outer-scaled wall-normal position in figure 5. A histogram of the height distribution is also included (grey bars) and marks the wall-normal extent of the roughness canopy ($h_{\min} < x_3 < h_{max}$). Looking from left-to-right across figures 5(*a–c*), it is clear that δU^+ remains approximately constant from the highest crest ($x_3/h_{max} = 1$) to the channel half-height ($x_3/\delta = 1$) for the majority of surfaces investigated here. Two exceptions are

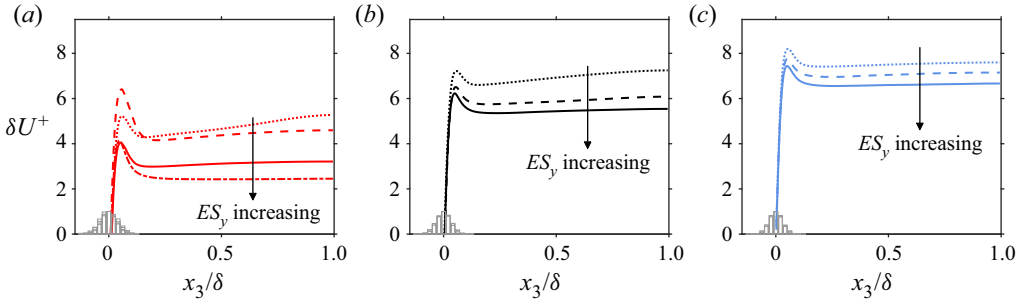

Figure 5. Streamwise velocity difference $\delta U^+(x_3) = \langle u_1^+ \rangle_s - \langle u_1^+ \rangle_r$ plotted as a function of wall-normal position for (*a*) Group A, (*b*) Group B, and (*c*) Group C. The histogram (grey) for each height distribution $P(h)$ is included for reference. All data are scaled using the mean friction velocity u_τ and mean channel half-height δ.

surface 022_010 (black dotted line in figure 5*b*) and surface 010_010 (red dotted line in figure 5*a*), with the latter surface showing an increase of almost 15 % when comparing the value of δU^+ at the channel half-height against that of the roughness crest. To remove any ambiguity related to variations of δU^+ in the outer region, ΔU^+ is herein defined as the mean value of the streamwise velocity difference between the highest roughness crest and the channel half-height, $\Delta U^+ \equiv 1/(\delta - h_{max}) \int_{h_{max}}^{\delta} \delta U^+(x_3)\, \mathrm{d}x_3$. Other definitions of ΔU^+ are possible: Chan *et al.* (2015) defined ΔU^+ as the streamwise velocity difference 50 wall units above the roughness crests in rough-wall turbulent pipe flow, whereas Busse *et al.* (2015) defined ΔU^+ as the streamwise velocity difference at the centreline in rough-walled turbulent channel flow; Chung *et al.* (2015) defined ΔU^+ as the streamwise velocity difference at wall-normal height $z_c = 0.4L_3$ in rough-wall minimal open-channel flow.

The Hama roughness function is plotted as a function of ES_y in figure 6(*a*). Three key observations can be drawn from these data. First, ΔU^+ varies by a factor of three ($2.5 < \Delta U^+ < 7.6$) for the ten roughness topographies investigated here. Second, ΔU^+ decreases monotonically as ES_y increases for each value of ES_x. Third, ΔU^+ becomes increasingly sensitive with respect to ES_y as ES_x is reduced. To be specific, whereas increasing ES_y from 0.10 to 0.35 reduces ΔU^+ by 12 % for surfaces with $ES_x \approx 0.35$ (blue symbols, Group C, figure 6*a*), a 35 % reduction is observed for surfaces with $ES_x \approx 0.10$ for the same change of ES_y (red symbols, Group C, figure 6*a*). A further 23 % reduction in the Hama roughness function is observed for surface 010_070 (red diamond, figure 6*a*) relative to that of surface 010_035 (red circle, figure 6*a*), resulting in a ΔU^+ value of just 2.4 wall units for the latter riblet-like surface. Together, these three observations demonstrate that ES_y is an important topographical parameter, particularly for lower-ES_x surfaces.

The Hama roughness function is plotted against ES_x in figure 6(*b*). In line with the findings of Napoli *et al.* (2008) and others, increasing ES_x from 0.10 to 0.35 causes ΔU^+ to increase for each value of ES_y considered here. However, it is important to note that ΔU^+ may show the opposite trend for higher-ES_x surfaces that fall within the dense regime (MacDonald *et al.* 2016). The Hama roughness function is plotted against the effective slope ratio ES_y/ES_x in figure 6(*c*), where data points from Busse & Jelly (2020) have been included for comparison. Despite their differing ES_x and ES_y combinations, a reasonable collapse between the two datasets is observed, and most of the ΔU^+ values

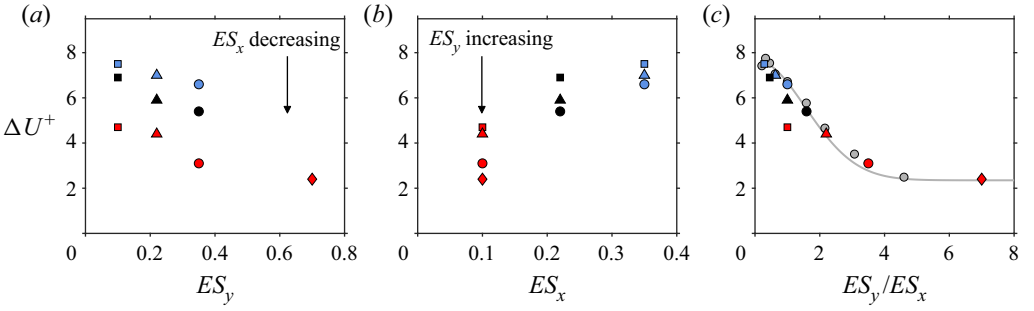

Figure 6. Hama roughness function ΔU^+ plotted as a function of (*a*) spanwise effective slope, ES_y, (*b*) streamwise effective slope ES_x, (*c*) ratio of spanwise and streamwise effective slopes ES_y/ES_x. Data points from the past work of Busse & Jelly (2020) are also included (grey circles) for comparison, along with an an exponential fit (grey line) of the form $\Delta U^+ = b_1 + b_2 \exp[-b_3(ES_y/ES_x)^2]$, where $b_i = \{2.35, 5.33, 0.207\}$. Symbol types are given in table 3.

exhibit a similar dependence upon ES_y/ES_x. To be specific, the relationship between ΔU^+ and ES_y/ES_x can be approximated as an exponential function of the form $\Delta U^+ = b_1 + b_2 \exp[-b_3(ES_y/ES_x)^2]$, where the coefficients $b_i = \{2.35, 5.33, 0.207\}$ were determined via nonlinear regression. A similar dependence between ΔU^+ and the SAR parameter was reported by Busse & Jelly (2020). Whilst figure 6(*c*) shows that ΔU^+ varies significantly across the range $0.3 \lesssim ES_y/ES_x < 7.0$ for a fixed value of k^+, predicting the limiting behaviour of ΔU^+ using the available data remains challenging. For instance, for the case where $ES_y/ES_x \to \infty$ with $ES_x = 0$ and very low ES_y, ΔU^+ would likely tend to zero, since this ES_x–ES_y combination corresponds to an almost smooth surface. On the other hand, for $ES_y/ES_x \to \infty$ with $ES_x = 0$ and high ES_y, it is possible that $\Delta U^+ \neq 0$, since this ES_x–ES_y combination corresponds to a riblet-like surface, which could either increase or decrease the levels of (viscous) drag; e.g. see Gatti *et al.* (2020). Also, since the data in figure 6(*c*) correspond for a fixed viscous-scaled roughness height $k^+ \approx 65.8$, questions regarding how the limiting behaviour of ΔU^+ varies with roughness Reynolds number remain open.

Nevertheless, figure 6(*c*) demonstrates that the Hama roughness function is sensitive with respect to surface anisotropy and gives insight into how ES_y/ES_x affects ΔU^+ at a fixed roughness Reynolds number $k^+ \approx 65.8$. Whilst ΔU^+ values have been obtained for a variety of anisotropic roughness in past work by Thakkar *et al.* (2016) and Jouybari *et al.* (2021), these studies not only were performed at different k^+ values compared to the present study, but also did not eliminate the potential effects of other key topographical parameters upon the drag penalty, e.g. skewness, or vary ES_y or ES_x in a systematic manner (see figure 2). As a result, a meaningful comparison against these past studies and the data plotted in figure 6(*c*) cannot be made. On the other hand, a direct comparison can be drawn against the past data of Busse & Jelly (2020) (filled grey circles, figure 6*c*), since that work was performed at the same k^+ value as the present study and focused on near-Gaussian roughness with comparable ES_x and ES_y combinations.

3.2. *Impact of spanwise effective slope upon pressure and viscous drag*

To associate physical mechanisms to changes in ΔU^+ (figure 6), the fractional contributions of pressure and viscous drag to the total drag can be quantified. After some manipulation, the mean viscous and pressure forces per unit area acting on the surface can

be written as

$$\langle F_v \rangle = \iint_S -\mu \left[2\,\frac{\partial \bar{u}_1}{\partial x_1}\,\frac{\partial h}{\partial x_1} + \left(\frac{\partial \bar{u}_1}{\partial x_2} + \frac{\partial \bar{u}_2}{\partial x_1} \right) \frac{\partial h}{\partial x_2} - \left(\frac{\partial \bar{u}_1}{\partial x_3} + \frac{\partial \bar{u}_3}{\partial x_1} \right) \right] \frac{1}{\|\nabla h\|}\,\mathrm{d}S, \quad (3.1)$$

$$\langle F_p \rangle = \iint_S \left[(\bar{p}_s - \bar{p}_0)\,\frac{\partial h}{\partial x_1} \right] \frac{1}{\|\nabla h\|}\,\mathrm{d}S. \quad (3.2)$$

In (3.1) and (3.2), $\bar{p}_0$ is an arbitrary gauge pressure, taken here as the mean surface pressure, i.e. $\bar{p}_0 \equiv A^{-1} \iint \bar{p}_s(x_1, x_2)\,\mathrm{d}A$, $\|\nabla h\|$ is the magnitude of the surface normal vector, and $\mathrm{d}S$ is the incremental surface area. Further details regarding (3.1) and (3.2) are provided in Appendix B.

Since the present simulations were carried out under constant pressure gradient forcing, the mean hydrodynamic force balance can be expressed as $\langle F_p \rangle + \langle F_v \rangle = 1$ (where $\Pi = -1$). Hence the summed effect of pressure and viscous drag remains constant, but the relative contributions of $\langle F_p \rangle$ and $\langle F_v \rangle$ to the total drag force, $\langle F_{tot} \rangle \equiv \langle F_p \rangle + \langle F_v \rangle = 1$, are free to vary. In the limit of streamwise homogeneous roughness ($ES_x \to 0$), pressure drag is equal to zero, and the force balance for the current channel flow configuration reduces to $-\Pi = \iint_S -\mu[(\partial \bar{u}_1/\partial x_2)(\partial h/\partial x_2) - \partial \bar{u}_1/\partial x_3](1/\|\nabla h\|)\,\mathrm{d}S$, which shows that changes in spanwise gradient of the height map, and hence changes in ES_y, influence directly the levels of viscous drag. The same force balance governs the drag-increasing (or drag-reducing) properties of other streamwise homogeneous surfaces, e.g. flow-aligned riblets (Gatti *et al.* 2020). Conversely, in the limit of spanwise homogeneous roughness ($ES_y \to 0$), the force balance for the current channel flow configuration reduces to $-\Pi = \iint_S -\mu[2(\partial \bar{u}_1/\partial x_1)(\partial h/\partial x_1) - (\partial \bar{u}_1/\partial x_3 + \partial \bar{u}_3/\partial x_1)](1/\|\nabla h\|) + [(\bar{p}_s - \bar{p}_0)(\partial h/\partial x_1)](1/\|\nabla h\|)\,\mathrm{d}S$, and is therefore independent of ES_y by definition. For the present surfaces, the relative importance of pressure and viscous drag sits somewhere between these two limits.

The fractional contribution of spatially averaged pressure drag to the total drag force, $\langle F_p \rangle / \langle F_{tot} \rangle$, is plotted against ES_y and ES_x in figures 7(*a*,*b*), respectively. Overall, the pressure drag data show the same trends as the corresponding ΔU^+ data plotted in figure 6. In summary, $\langle F_p \rangle / \langle F_{tot} \rangle$ decreases as ES_y increases for each value of ES_x investigated here, and exhibits a heightened sensitivity with respect to ES_y as ES_x becomes smaller. Likewise, when $\langle F_p \rangle / \langle F_{tot} \rangle$ is plotted against ES_y/ES_x (figure 7*c*), the pressure drag contribution decreases as ES_y/ES_x increases, meaning that streamwise-elongated forms of surface roughness ($ES_y/ES_x > 1$) induce less pressure drag than their spanwise-aligned counterparts ($ES_y/ES_x < 1$). Note that the fractional contribution of spatially averaged viscous drag to the total drag force would show exactly the opposite trends, since $\langle F_v \rangle \equiv 1 - \langle F_p \rangle$ for constant pressure gradient forcing.

The fractional contribution of pressure drag is plotted as a function of ΔU^+ in figure 7(*d*). The data show that $\langle F_p \rangle / \langle F_{tot} \rangle$ varies by up to a factor of seven within the observed ΔU^+ range. Specifically, pressure drag accounts for just 10 % ($\langle F_p \rangle / \langle F_{tot} \rangle \approx 0.1$) of the total drag on surface 010_070 (red diamond, figure 7*d*), compared to 74 % of the total drag ($\langle F_p \rangle / \langle F_{tot} \rangle \approx 0.74$) on surface 035_010 (blue square, figure 7*d*). Whilst the dependence of $\langle F_p \rangle / \langle F_{tot} \rangle$ on ES_x is well-documented (Napoli *et al.* 2008; MacDonald *et al.* 2016; Chan *et al.* 2018), the present data show that the fractional contribution of pressure drag ratio also depends on ES_y. However, a strong sensitivity with respect to ES_y is expected only if the total wall drag has an appreciable viscous component. This is because the impact of spanwise variations in surface elevation, and hence variations in ES_y, upon hydrodynamic drag are transmitted through the viscous term (see (3.1)),

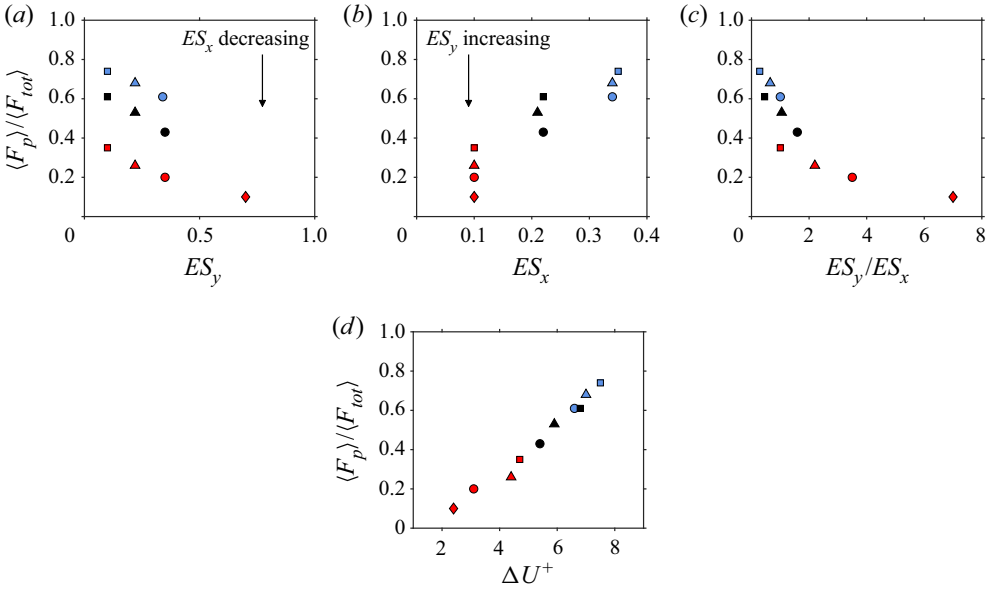

Figure 7. Fractional contribution of spatially averaged pressure drag to the total drag force, $\langle F_p\rangle/\langle F_{tot}\rangle$, plotted as a function of: (*a*) spanwise effective slope ES_y; (*b*) streamwise effective slope ES_x; (*c*) ratio of spanwise and streamwise effective slopes, ES_y/ES_x; and (*d*) the Hama roughness function ΔU^+. Symbol types are given in table 3.

which becomes increasingly small as the fully rough asymptote is approached. In other words, limited sensitivity with respect to ES_y is to be expected when $\langle F_p\rangle \gg \langle F_v\rangle$.

Different criteria have been established in the literature to establish whether flow over a rough surface is in the fully rough regime. According to Scaggs, Taylor & Coleman (1988), the onset of the fully rough regime occurs when pressure drag accounts for more than 70 % of the total drag, i.e. $F_p/F_{tot} > 0.7$, meaning that only surface 035_010 in the present investigation should be considered fully rough (see figure 7). Jiménez (2004) defined the onset of the fully rough regime at $k_s^+ > 80$, which corresponds to a Hama roughness function $\Delta U^+_{FR} = \kappa^{-1}\log(k_s^+) - 3.5 \approx 7.5$ (assuming $\kappa = 0.4$). Again, based on this criterion, only surface 035_010 should be considered fully rough (see figure 6) – nevertheless, its viscous drag is non-negligible at 25 %. Past work has also reported significant viscous effects in flows that exhibit fully rough behaviour. For instance, MacDonald, Hutchins & Chung (2019) reports that viscous drag still accounts for a quarter of the total drag in fully rough turbulent channel flow over three-dimensional egg-carton roughness at friction Reynolds number $Re_\tau = 1680$, corresponding to an equivalent sand-grain roughness $k_s^+ = 300$. Likewise, Busse, Thakkar & Sandham (2017) considered turbulent channel flow over irregular roughness up to friction Reynolds number $Re_\tau = 720$. These authors reported that viscous effects account for approximately 33 % of the total drag at an equivalent sand-grain roughness $k_s^+ \approx 150$. Nevertheless, the majority of the present data fall into the transitionally rough regime.

To better understand how varying ES_y affects the ratio $\langle F_p\rangle/\langle F_{tot}\rangle$ on Group A surfaces, the local values of time-averaged pressure drag can be examined. Contour plots of the time-averaged pressure drag on the four surfaces belonging to Group A surfaces are shown in figure 8. Whereas large patches of high-pressure drag (red

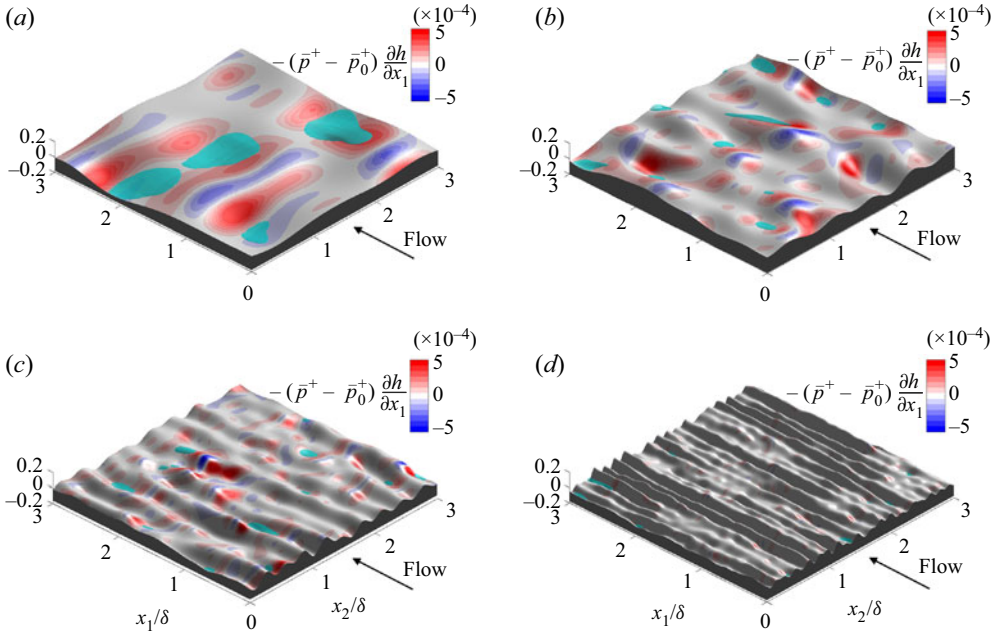

Figure 8. Time-averaged pressure drag force $-(\bar{p}^+ - \bar{p}_0^+)\partial h/\partial x_1$ (the integrand of term $\langle F_p \rangle$ in (3.2)) for surfaces (*a*) 010_010, (*b*) 010_022, (*c*) 010_035, and (*d*) 010_070. Iso-surfaces of time-averaged reverse flow ($\bar{u}_1^+ = -0.1$) are shown as transparent cyan blobs. Data are shown on a $(3 \times 3)/\delta$ sub-tile, where δ is the mean channel half-height.

contours) and low-pressure drag (blue contours) are evident on the windward and leeward faces of surfaces 010_010 and 010_022 (figures 8*a*,*b*), the pressure drag distribution on surfaces 010_035 and 010_070 (figures 8*c*,*d*) is comparably weak and sparse. A simple explanation for this behaviour is that the streamwise component of the surface normals on streamwise-elongated roughness tend to be small, and as a result, a weaker pressure drag force is exerted against the wall. The integrated effect of this behaviour explains why $\langle F_p \rangle / \langle F_{tot} \rangle$ decreases as ES_y increases (figure 7*b*) and also why pressure drag decreases as ES_y/ES_x increases (figure 7*c*). Iso-surfaces of time-averaged reverse flow are also included as transparent cyan blobs in figure 8. The volume of the time-averaged reverse flow regions decreases as ES_y increases, which implies that flow separation downwind of roughness crests is suppressed for flow-aligned roughness, ultimately reducing the fractional contribution of spatially averaged pressure drag to the total drag (see figure 7*d*).

The bulk flow properties for the rough- and smooth-wall cases are summarised in table 4. Since the friction Reynolds number is equal to 395 for all cases, the rise in the mean momentum deficit can be inferred from a reduction of the bulk Reynolds number Re_b or the centreline Reynolds number Re_{cl}, or an increase in the Hama roughness function ΔU^+. Recalling that each surface considered here has a common mean peak-to-valley height and a near-Gaussian height distribution (table 2), the bulk properties listed in table 4, together with the variation of the Hama roughness function (figure 6) and the fractional contribution of spatially averaged pressure drag (figure 7), demonstrate that ES_y is an important topographical parameter – particularly for low-ES_x surfaces. Next, the impact of ES_y upon first-order velocity statistics will be examined.

	ID code	Re_τ	Re_{cl}	Re_b	U_{cl}^+	U_b^+	$\frac{U_{cl}}{U_b}$	ΔU^+	C_f ($\times 10^{-3}$)	$\frac{\langle F_p \rangle}{\langle F_{tot} \rangle}$
A	010_070	395	7082	5936	17.9	15.0	1.19	2.4	8.85	0.10
	010_035	395	6782	5751	17.2	14.6	1.18	3.1	9.43	0.20
	010_022	395	6233	5131	15.8	13.0	1.21	4.4	11.85	0.26
	010_010	395	5968	5024	15.1	12.7	1.19	4.7	12.36	0.35
B	022_035	395	5862	4977	14.8	12.2	1.22	5.4	13.52	0.43
	022_022	395	5684	4633	14.3	11.7	1.22	5.9	14.53	0.53
	022_010	395	5186	4234	13.1	10.7	1.22	6.9	17.40	0.61
C	035_035	395	5431	4345	13.8	11.0	1.25	6.6	16.52	0.61
	035_022	395	5226	4175	13.2	10.6	1.25	7.0	17.90	0.68
	035_010	395	5048	3997	12.8	10.1	1.26	7.5	19.53	0.74
—	Smooth	395	8050	6928	20.4	17.5	1.16	—	6.50	—

Table 4. Bulk flow properties, including the friction Reynolds number Re_τ, centreline Reynolds number $Re_{cl} \equiv U_{cl}\delta/\nu$, bulk Reynolds number $Re_b \equiv U_b\delta/\nu$, viscous-scaled centreline velocity (U_{cl}^+), viscous-scaled bulk velocity U_b^+, ratio of centreline and bulk velocities U_{cl}/U_b; Hama roughness function ΔU^+; skin-friction coefficient $C_f \equiv 2/(U_b^{+2})$; and fractional contribution of spatially averaged pressure drag to total drag, $\langle F_p \rangle / \langle F_{tot} \rangle$.

3.3. *Impact of spanwise effective slope on first-order velocity statistics*

Double-averaged (DA) streamwise velocity profiles normalised by the mean friction velocity are plotted against inner-scaled wall-normal position in figure 9, where reference smooth-wall data at matched flow conditions are included for comparison. Looking from left to right across figures 9(*a–c*), it is clear that most of the data exhibit a (nominal) log-law of the form

$$\langle \bar{u}_1^+ \rangle = \kappa^{-1} \log\left(x_3^+ + \epsilon\right) + B - \Delta U^+, \tag{3.3}$$

where $\kappa \approx 0.4$ is the von Kármán constant, ϵ is the virtual origin shift, and $B \approx 5.0$ is the smooth-wall intercept. Note that the virtual origin shift of the DA velocity profile was chosen to coincide with the mean roughness plane, i.e. $\epsilon \equiv \langle h \rangle = 0$. This choice of ϵ is consistent with past studies of turbulent channel flow with irregular rough walls with comparable values of ES_x and ES_y (Thakkar *et al.* 2016; Peeters & Sandham 2019; Portela *et al.* 2021), as well as studies of turbulent pipe flow over three-dimensional egg-carton roughness (Chan *et al.* 2015, 2018).

In line with the values of ΔU^+ shown in figure 6, the downward shift of the log-law observed in figure 9 decreases as ES_y increases for each value of ES_x investigated here. However, whilst the velocity profiles exhibit a logarithmic dependence over the wall-normal range $50 \lesssim x_3^+ \lesssim 200$, the slope of the log region above some surfaces appears to differ from the smooth-wall data. In particular, the log region for surfaces 010_010 (red dotted line in figure 9*a*) and 022_010 (black dotted line in figure 9*b*) exhibit a shallower slope than the reference smooth-wall data (grey line), which is consistent with the non-uniform streamwise velocity difference observed previously in figure 5(*a*).

A further evaluation of the DA streamwise velocity profiles using the log-law diagnostic quantity $\gamma = x_3^+ \, \mathrm{d}\langle \bar{u}_1 \rangle / \mathrm{d}x_3^+$ (George 2007) is presented in figure 10. Whilst an extensive log region is not evident in the current data, the diagnostic function shows consistent behaviour with the outer region of the DA streamwise velocity profiles (see figure 9). To be specific, the log-law diagnostic function for Group C shows limited sensitivity

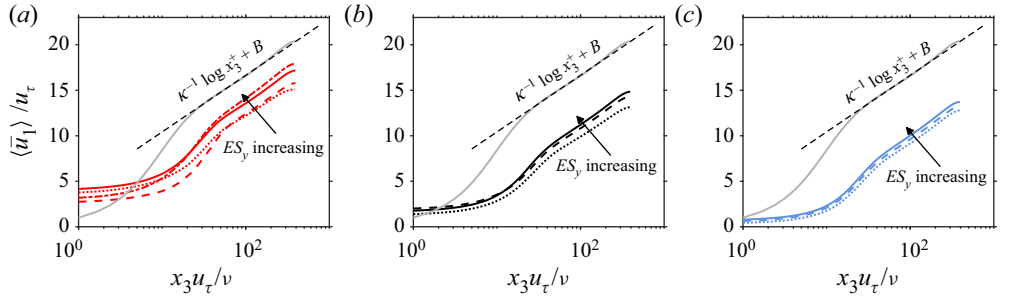

Figure 9. Effect of varying ES_y upon the DA inner-scaled streamwise velocity profile $\langle u_1 \rangle^+(x_3)$ for surfaces in (*a*) Group A, (*b*) Group B, and (*c*) Group C. Line types are defined in table 3. The smooth-wall log-law $\kappa^{-1} \log x_3^+ + B$ is also included, where $\kappa = 0.4$ and $B = 5.0$.

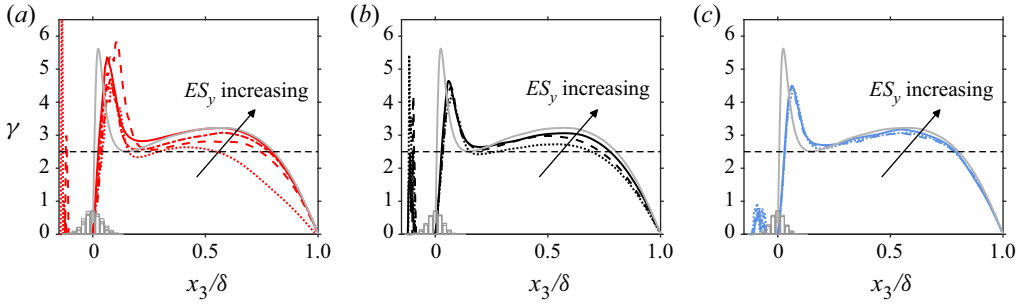

Figure 10. Effect of varying ES_y upon the log-law diagnostic function $\gamma = x_3^+ \, \mathrm{d}\langle \bar{u}_1 \rangle / \mathrm{d}x_3^+$, for (*a*) Group A, (*b*) Group B, and (*c*) Group C surfaces. The histogram for each height distribution $P(h)$ is included for reference in grey. The horizontal black dashed line corresponds to $\gamma = 1/\kappa$, where κ was taken to be 0.4. Line types are defined in table 3.

with respect to ES_y, whereas Group A shows the opposite trend. In addition, whilst the log-law diagnostic function for Group C resembles the smooth-wall data in the outer region, appreciable differences emerge above Group A and B surfaces, which become more pronounced as ES_y is reduced. Together, the change in the log-law slope above surfaces 010_010 (red dotted line in figure 9*a*) and 022_010 (black dotted line in figure 9*b*), and the deviations between the smooth- and rough-wall log-law diagnostic functions in the outer region (figure 10), hint at the presence of non-equilibrium effects and imply that the DA velocity profiles for these two particular surfaces may not recover mean flow outer-layer similarity.

To better illustrate the presence (or absence) of mean flow outer-layer similarity, the DA velocity profiles (figure 9) were recast into velocity-defect form,

$$\frac{\langle u_1 \rangle_{cl} - \langle u_1 \rangle}{u_\tau} = f\left(\frac{x_3}{\delta}\right), \tag{3.4}$$

where f is a universal function assumed independent of the viscous-scaled surface condition. While outer-layer similarity is typically investigated in the context of high-Reynolds-number flows and low k/δ using experimental methods (see e.g. Flack, Schultz & Shapiro 2005), many DNS studies at more moderate Reynolds numbers and comparatively high k/δ ratios have also observed a high degree of outer-layer similarity (Chan *et al.* 2015; Thakkar *et al.* 2016; Forooghi *et al.* 2018*b*; Jelly & Busse 2019*b*).

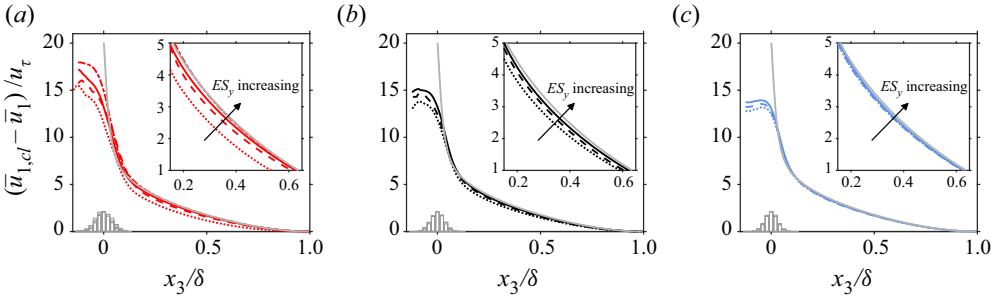

Figure 11. Effect of varying ES_y upon DA streamwise velocity defect profile $\langle u_{1,cl}\rangle^+ - \langle u_1\rangle^+(x_3)$ for (*a*) Group A, (*b*) Group B, and (*c*) Group C surfaces. The histogram for each height distribution $P(h)$ is included for reference in grey. Line types are defined in table 3.

However, k/δ and Re_τ are not the only length scale ratios that determine the degree of outer-layer similarity. Specifically, there is a growing body of literature showing that diminished levels of outer-layer similarity emerge when the in-plane spanwise roughness length scale approaches δ – including experimental investigations where low k/δ and high Re_τ could be achieved; e.g. see work by Nugroho, Hutchins & Monty (2013), Wangsawijaya *et al.* (2020) and Nugroho *et al.* (2021). Such scenarios are possible for particular low-ES_y surfaces considered in the present study, e.g. surface 010_010 whose in-plane spanwise roughness length scale is almost twice as large as the channel half-height, i.e. $\overline{\lambda_y}/\delta \approx 2$, as shown in figure 4).

DA velocity defect profiles are plotted against outer-scaled wall-normal position in figure 11, where reference smooth-wall data at matched flow conditions are included for comparison. Looking from left to right across figures 11(*a–c*), it is clear that Group C (blue lines, figure 11*c*) data show excellent levels of outer-layer similarity, and that varying ES_y has little to no effect on the flow in the outer region (see inset of figure 11(*c*) for a close-up view). Group C data are therefore in strong support of Townsend's outer-layer similarity hypothesis (Townsend 1976), which states that the roughness merely increases the surface stress, without causing structural changes in the outer region. In contrast, Group A data (red lines, figure 11*a*) show progressively poor levels of mean flow outer-layer similarity as ES_y is reduced. In particular, the velocity-defect profile for surface 010_010 (red dotted line, figure 11*a*) begins to coincide with the smooth-wall data only above wall-normal heights greater than $x_3/\delta \gtrsim 0.8$ – implying that roughness effects penetrate deep into the outer layer, and mean flow distortion occurs on a scale commensurate with the channel half-height δ. Diminished levels of mean flow outer-layer similarity have also been reported in recent studies above multi-scale cuboid elements (Medjnoun *et al.* 2021) and above irregular roughness with $ES_x = ES_y \approx 0.08$ (Nugroho *et al.* 2021). In both of these studies, reduced levels of outer-layer similarity were attributed to the emergence of large-scale roughness-induced motions on the cross-stream plane.

Contours of streamwise dispersive velocity $\tilde{u}_1(\boldsymbol{x}) \equiv \bar{u}_1(\boldsymbol{x}) - \langle u_1\rangle(x_3)$ are compared on the cross-stream plane for surfaces 010_010 and 010_070 in figures 12(*a*) and 12(*b*), respectively. Whereas the spanwise variation in the streamwise dispersive velocity is confined to wall-normal heights less than $x_3/\delta \lesssim 0.1$ above the latter surface, the former, lower-ES_y surface shows a markedly different behaviour. In particular, the spanwise variation in streamwise dispersive stress above surface 010_010 extends up to (and beyond) the channel half-height ($x_3/\delta = 1$), which implies that the portion of time-averaged flow with spatial inhomogeneity induced by the roughness elements (i.e. the roughness

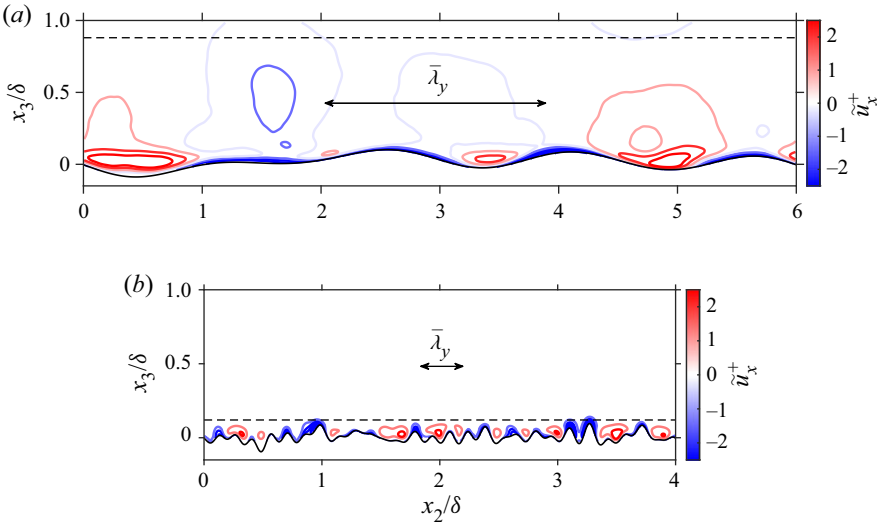

Figure 12. Effect of increasing ES_y upon cross-stream distribution of streamwise dispersive velocity $\tilde{u}_1(\boldsymbol{x}) \equiv \bar{u}_1(\boldsymbol{x}) - \langle u_1 \rangle(x_3)$ for (*a*) surface 010_010 at $x_1/\delta = 0.23$, and (*b*) surface 010_070 at $x_1/\delta = 4.78$. The mean spanwise wavelength $\bar{\lambda}_y$ is represented by the width of the horizontal double-headed arrow. The horizontal dashed line shows the approximate wall-normal extent of the dispersive stresses $x_3 = 0.5\bar{\lambda}_y$ proposed by Chan *et al.* (2018).

sublayer) fills the entire channel. Past work by Chan *et al.* (2018) suggests that dispersive stresses (see (2.7)) extend up to height $x_3 = 0.5\bar{\lambda}_y$ in the wall-normal direction. This limit is shown as the horizontal dashed line in figure 12, and predicts approximately the wall-normal extent of streamwise dispersive velocity above both surfaces 010_010 and 010_070.

Considering the impact that reducing ES_y has upon the thickness of the roughness sublayer (figure 12), the diminished level of outer-layer similarity above surface 010_010 is arguably caused by inadequate scale separation between $\bar{\lambda}_y$ and δ. More specifically, whilst the blockage ratio for surface 010_010 is $k/\delta = 1/6$ (where k is taken to be the mean peak-to-valley height $S_{z,5\times5}$), which is the same k/δ value used in past studies where good levels of outer-layer similarity were observed (Thakkar *et al.* 2016; Jelly & Busse 2018; Portela *et al.* 2021), the ratio between $\bar{\lambda}_y$ and δ is approximately twelve times greater ($\bar{\lambda}_y/\delta \approx 2$, red square, upper right quadrant of figure 4). On the other hand, the ratio between $\bar{\lambda}_y$ and δ is an order of magnitude smaller for surface 010_070 ($\bar{\lambda}_y/\delta \approx 0.2$, red diamond, lower right quadrant of figure 4), which shows negligible spanwise variation in streamwise dispersive velocity in the outer region (figure 12*b*) and excellent levels of outer-layer similarity (red dash-dot line, figure 9*a*). Considering also that the in-plane streamwise mean wavelengths on surfaces 010_010 and 010_070 both exceed the outer length scale, i.e. $\bar{\lambda}_x/\delta > 1$ (see figure 4), the diminished levels of outer-layer similarity above the former surface occur as a direct result of insufficient scale separation between $\bar{\lambda}_y$ and δ, as opposed to between $\bar{\lambda}_x$ and δ or between k and δ. This is consistent with recent work by Nugroho *et al.* (2021), who noted that the wall-normal extent of roughness-induced flow patterns becomes large relative to δ where the in-plane roughness length scale approaches the local boundary-layer thickness, ultimately limiting the overall levels of outer-layer similarity. However, that work focused on an isotropic

irregular roughness with $ES_x = ES_y \approx 0.08$ and the impact of varying $\bar{\lambda}_y$, and hence ES_y could not be delineated from its streamwise counterpart.

To further characterise roughness-induced motions on the cross-plane (figure 12), secondary flow patterns were educed from the time-averaged velocity field $\bar{u}_i(\boldsymbol{x})$ using a technique similar to that employed by Adrian, Christensen & Liu (2000) to identify instantaneous vortical structures on the streamwise-radial plane of turbulent pipe flow using planar particle image velocimetry data. The signed swirling strength, defined here as $\bar{\Lambda}_{ci} \equiv \lambda_{ci}(\bar{\omega}_1/|\bar{\omega}_1|)$, was computed by evaluating the imaginary component of the complex conjugate eigenvalue λ_{ci} of the two-dimensional time-averaged velocity gradient tensor, which can written as

$$\overline{\boldsymbol{d}}_{ij,2D}\,(x_2, x_3) = \begin{bmatrix} \dfrac{\partial \bar{u}_2}{\partial x_2} & \dfrac{\partial \bar{u}_2}{\partial x_3} \\ \dfrac{\partial \bar{u}_3}{\partial x_2} & \dfrac{\partial \bar{u}_3}{\partial x_3} \end{bmatrix} \tag{3.5}$$

on successive cross-stream planes. Note that $(\bar{\omega}_1/|\bar{\omega}_1|)$ is the sign of the time-averaged streamwise vorticity $\bar{\omega}_1(\boldsymbol{x}) = \partial\bar{u}_2/\partial x_3 - \partial\bar{u}_3/\partial x_2$. Hence $\Lambda_{ci} \neq 0$ indicates the presence of local (steady) vortical motion, with $\Lambda_{ci} > 0$ and $\Lambda_{ci} < 0$ corresponding to clockwise and counter-clockwise rotation, respectively.

Iso-surfaces of time-averaged signed swirling strength $\bar{\Lambda}_{ci}(\boldsymbol{x})$ for the four surfaces in Group A are shown in figure 13, where the value of ES_y increases from top to bottom. Data are visualised above a $(4 \times 4)/\delta$ sub-tile, where red iso-surfaces indicates clockwise rotation, and blue iso-surfaces indicates the opposite. Looking at figures 13(*a–d*), it is clear that the spatial characteristics of the time-averaged secondary flows are strongly affected by ES_y. For instance, the secondary flow patterns corresponding to surface 010_070 (figure 13*a*) strongly resemble the streamwise homogeneous counter-rotating vortex pairs that form above strip-type roughness (Yang & Anderson 2018) and are confined to wall-normal heights less than $x_3/\delta \lesssim 0.1$ in a manner similar to the cross-plane distribution of streamwise dispersive velocity (figure 12*b*). On the other hand, the secondary flow patterns above surface 010_010 (figure 13*d*) appear relatively incoherent in both the streamwise and spanwise directions, and extend far from the wall into the outer region of the flow, which, again, is consistent with the cross-plane distribution of streamwise dispersive velocity (figure 12*a*).

Overall, the observations drawn from figure 13 are consistent with recent studies regarding the formation of turbulent secondary flows over streamwise-aligned surfaces composed of spanwise alternating smooth and rough strips in channels (Yang & Anderson 2018), boundary layers (Wangsawijaya *et al.* 2020) and Taylor–Couette flows (Bakhuis *et al.* 2020). For this particular type of roughness, the (time-averaged) secondary flow behaviour is determined by the ratio of the spanwise wavelength $\bar{\lambda}_y = 2S$, where S is the width of the strips, and the local boundary layer thickness δ, and falls into one of three categories, e.g. see Chung, Monty & Hutchins (2018). (i) For $\bar{\lambda}_y/\delta \ll 0.5$ (or $S/\delta \ll 1$), the secondary flow is confined to the near-wall region and the flow is spanwise homogeneous above wall-normal heights greater than $x_3/\bar{\lambda}_y \approx 2$ (or $x_3/S \approx 1$), which is reminiscent of the cross-plane distribution of streamwise dispersive velocity above surface 010_070 (see figure 12*b*) and the corresponding iso-surfaces of signed swirling strength (see figure 13*a*). (ii) For $\bar{\lambda}_y/\delta \gg 2$ (or $S/\delta \gg 1$), the secondary flow is space-filling, characterised by δ-scale motions separated by regions of spanwise homogeneous flow. (iii) For $\bar{\lambda}_y/\delta \approx 2$ (or $S/\delta \approx 1$), the secondary flow is also space-filling, but the δ-scale motions occupy the entire cross-plane, which is reminiscent of the cross-plane distribution of streamwise dispersive

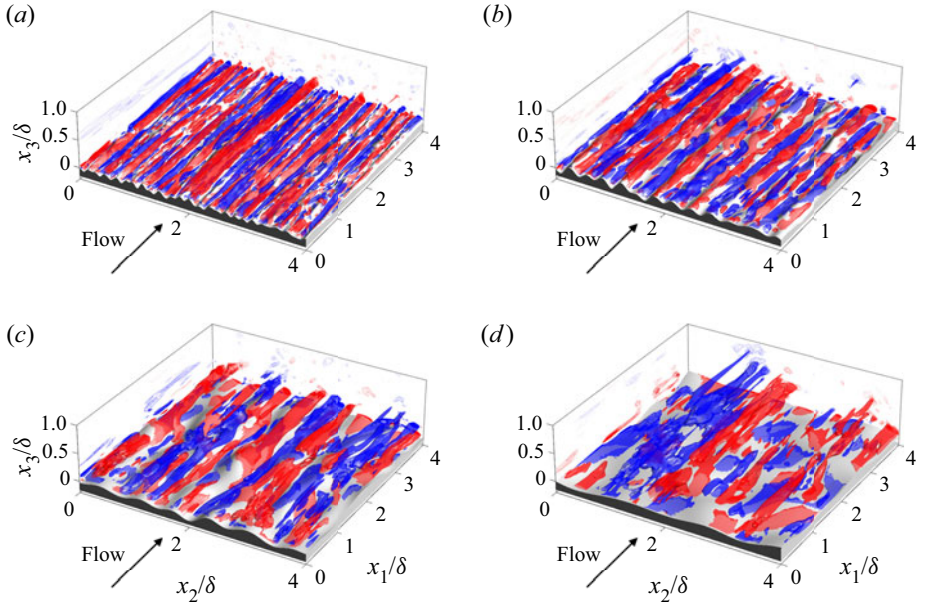

Figure 13. Effect of increasing ES_y upon iso-surfaces of the time-averaged signed swirl strength $\bar{\Lambda}_{ci} = 0.005$ (red) and $\bar{\Lambda}_{ci} = -0.005$ (blue), for surfaces (*a*) 010_070, (*b*) 010_035, (*c*) 010_022, and (*d*) 010_010. Data are shown on a $(4 \times 4)/\delta$ sub-tile, where δ is the mean channel half-height.

velocity above surface 010_010 (see figure 12*a*) and the corresponding iso-surfaces of signed swirling strength (see figure 13*d*). Considering (i)–(iii), the present data suggest that the ratio $\bar{\lambda}_y/\delta$ plays an analogous role in determining secondary flow behaviour above the irregular three-dimensional roughness under investigation here.

3.4. *Impact of spanwise effective slope on second-order velocity statistics*

To further understand how ES_y affects the wall-normal extent of roughness-induced flow patterns, dispersive stresses were computed and examined. Dispersive stresses represent momentum flux in the near-roughness region due to spatial heterogeneity in the time-averaged flow, and arise as a direct result of time-then-space averaging (Pokrajac, McEwan & Nikora 2008) (see (2.7)). Profiles of the dispersive normal stresses normalised by the square of the mean friction velocity are plotted against outer-scaled wall-normal position in figure 14. Whist the dynamical significance of 'form-induced' stress in the near-wall region is well-documented (Moltchanov, Bohbot-Raviv & Shavit 2011; Ma *et al.* 2021), it is often assumed to vanish in the outer layer (Meyers, Ganapathisubramani & Cal 2019). Looking from left to right across figure 14, it is clear that whilst the magnitude of the spanwise dispersive stress D_{22} is effectively zero in the outer region for all surfaces considered here (figures 14*d–f*), the remaining streamwise D_{11} and wall-normal D_{33} stresses do not necessarily follow the same trend. In particular, the latter component shows persistent levels well into the outer region for surface 010_010 (red dotted line in figure 14*a*), surface 010_022 (red dashed line in figure 14*a*), and, to a slightly lesser extent, surface 022_010 (black dotted line in figure 14*b*). These are the same three low-ES_y surfaces that exhibit a non-uniform streamwise velocity difference in the outer region (figure 5), non-universal coefficients in their respective log laws (figure 9), and diminished

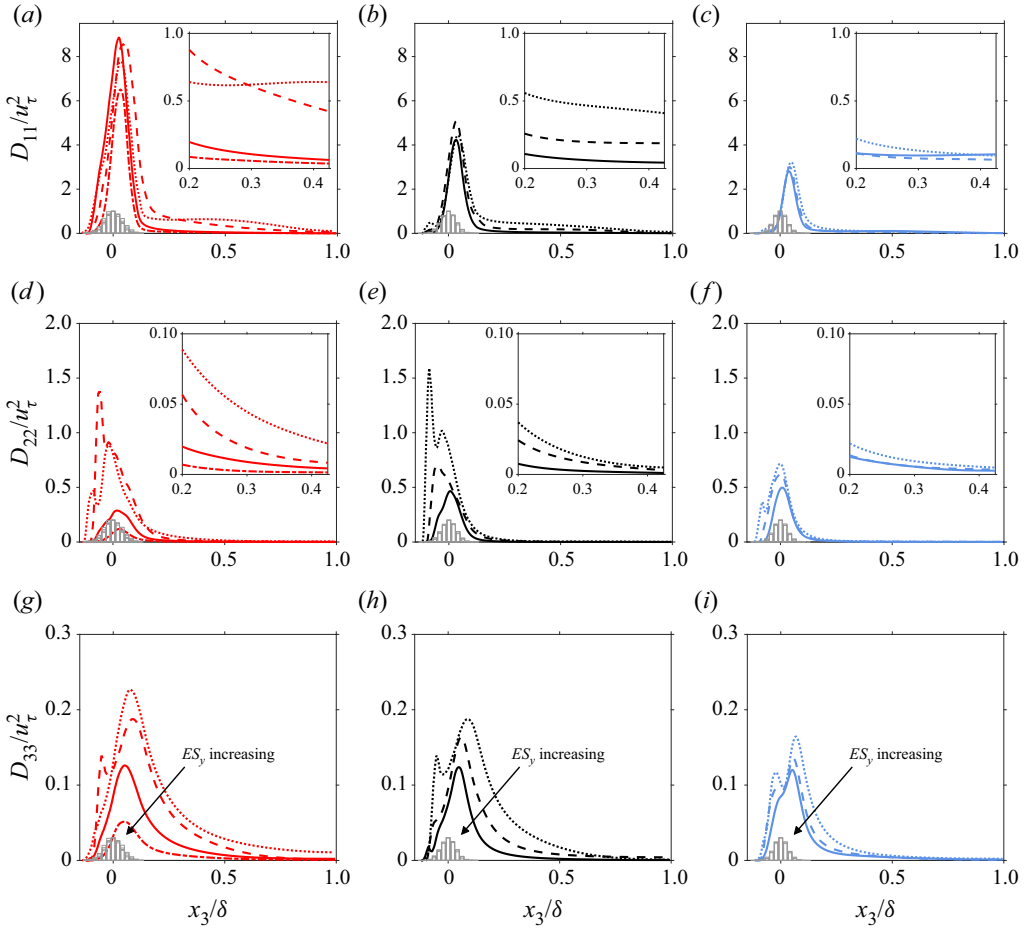

Figure 14. Effect of varying ES_y upon dispersive normal stresses $\boldsymbol{D}_{ii}(x_3)$. Streamwise dispersive stresses $D_{11}(x_3)$ for (*a*) Group A, (*b*) Group B, and (*c*) Group C surfaces. Spanwise dispersive stresses $D_{22}(x_3)$ for (*d*) Group A, (*e*) Group B, and (*f*) Group C surfaces. Wall-normal dispersive stresses $D_{33}(x_3)$ for (*g*) Group A, (*h*) Group B, and (*i*) Group C surfaces. The histogram for each height distribution $P(h)$ is included for reference in grey. Line types are defined in table 3.

levels of outer-layer similarity (figure 11), which again underlines the growing significance of ES_y as ES_x becomes smaller. In addition, the wall-normal persistence of dispersive stresses observed in figure 14 challenges the classical picture of an outer layer that is dominated by Reynolds stresses (Castro 2007) and therefore motivates an analysis of second-order turbulence statistics.

Profiles of spatially averaged streamwise Reynolds stress $\langle R_{11} \rangle$ normalised by the square of the mean friction velocity are plotted against outer-scaled wall-normal position for Groups A, B and C in figure 15. Looking from left to right across figures 15(*a–c*), it is clear that the best collapse between the smooth- and rough-wall data is observed for Group C (blue lines). These data are therefore in strong support of Townsend's outer-layer similarity hypothesis (Townsend 1976), which states that the turbulent stresses, normalised by the square of the mean friction velocity, are universal outside the roughness sublayer,

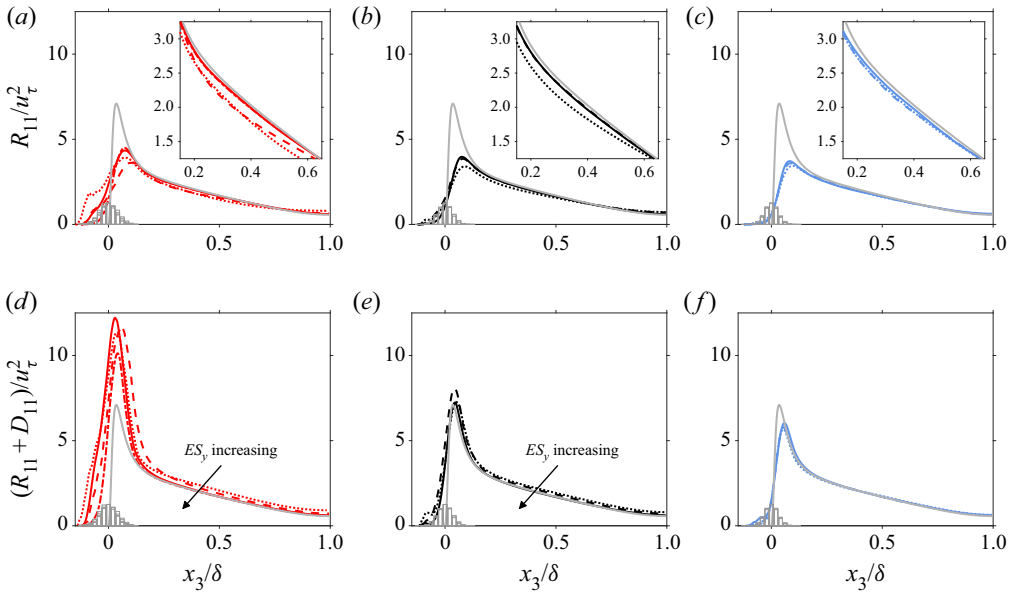

Figure 15. Effect of varying ES_y upon spatially averaged streamwise Reynolds stresses $\langle R_{11}\rangle(x_3)$ for (*a*) Group A, (*b*) Group B, and (*c*) Group C surfaces. Effect of varying ES_y upon the sum of spatially averaged streamwise Reynolds stress and streamwise dispersive stress, $\langle R_{11}\rangle(x_3) + D_{11}(x_3)$, for (*d*) Group A, (*e*) Group B, and (*f*) Group C surfaces. The histogram for each height distribution $P(h)$ is included for reference in grey. Line types are defined in table 3.

which can be written as

$$\frac{\langle \boldsymbol{R}_{ij}\rangle}{u_\tau^2} = g_{ij}\left(\frac{x_3}{\delta}\right), \tag{3.6}$$

where g_{ij} is a universal function hypothesised to be independent of the viscous-scaled surface condition. On the other hand, the streamwise Reynolds stress profile above surface 010_010 (dotted red line, figure 15*a*) and surface 010_022 (dotted black line, figure 15*b*) shows the worst overall collapse with the smooth-wall data, which is consistent with the behaviour of the log-law diagnostic functions (see figure 10) and velocity defect profiles (see figure 11). As was mentioned previously, one explanation for this behaviour is that as $\bar{\lambda}_y$ approaches δ, the roughness sublayer thickens, ultimately perturbing streamwise velocity fluctuations from their 'equilibrium' state. Past work has also reported diminished levels of outer-layer similarity on Reynolds stresses above roughness with long wavelength features in the spanwise direction – the limiting case being two-dimensional spanwise bars with $\bar{\lambda}_y/\delta \to \infty$. For instance, Volino, Schultz & Flack (2011) reported a breakdown of outer-layer similarity for Reynolds stresses in turbulent boundary-layer flow over two-dimensional bar roughness, but not for three-dimensional cube roughness, despite the latter being a factor three times larger than the smallest bars in terms of k. Although the roughnesses considered by Volino *et al.* (2011) have a fundamentally different character compared to the irregular, three-dimensional roughness under consideration in the present study – e.g. the former have fixed separation points whereas the latter does not – there is qualitative similarity in the sense that when ES_y becomes low (and spanwise features become large), the roughness sublayers thicken, which, ultimately, may lead to a breakdown of outer-layer similarity.

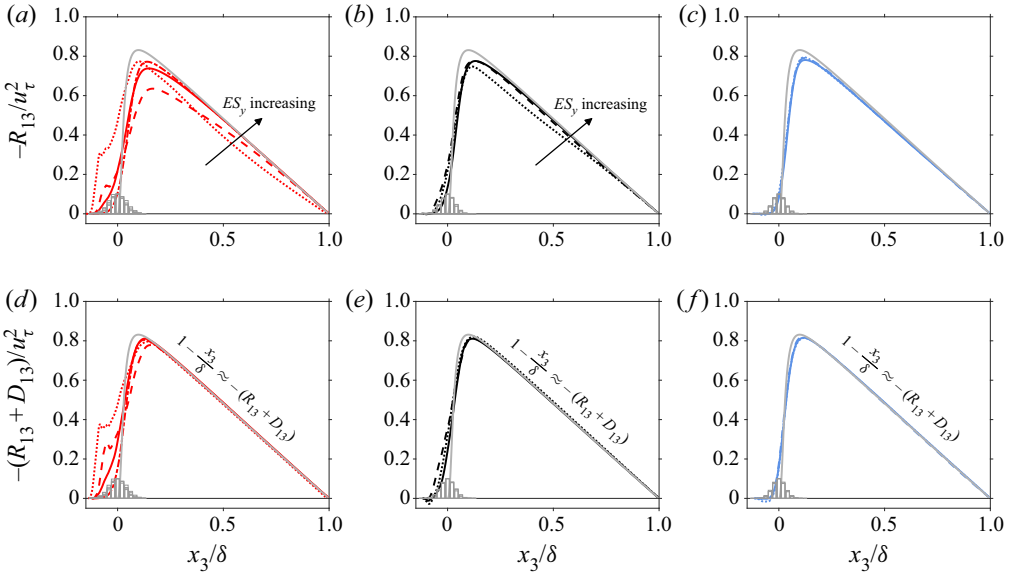

Figure 16. Effect of varying ES_y upon spatially averaged Reynolds shear stress $\langle R_{13}\rangle(x_3)$ for (*a*) Group A, (*b*) Group B, and (*c*) Group C surfaces. Effect of varying ES_y upon the sum of spatially averaged Reynolds shear stress and dispersive shear stress, $\langle R_{13}\rangle(x_3) + D_{13}(x_3)$, for (*d*) Group A, (*e*) Group B, and (*f*) Group C surfaces. The histogram for each height distribution $P(h)$ is included for reference in grey. Line types are defined in table 3.

Profiles of the sum of the spatially averaged Reynolds stress and streamwise dispersive stress, $\langle R_{11}\rangle + D_{11}$, for Groups A, B and C are shown in figures 15(*d–f*). Comparing these data against their Reynolds stress counterparts in (*a–c*), it is clear that observed levels of outer-layer similarity above Group C surfaces remain unaffected by the addition of streamwise dispersive stress, since D_{11} decays to a negligible value in the outer region (see figure 14*c*). This observation is consistent with the results of Forooghi *et al.* (2018*b*) and Busse & Jelly (2020), which show that D_{11} becomes negligible relative to $\langle R_{11}\rangle$ in the outer layer. In contrast, since D_{11} remains non-negligible above surface 010_010 (red dotted line, figure 14*a*) and surface 022_010 (black dotted line, figure 14*b*) well into the outer layer, the profiles of $\langle R_{11}\rangle + D_{11}$ shift upwards, relative to the Reynolds stress profiles plotted in figure 15(*a*), and fail to collapse on the smooth-wall data at all wall-normal positions (red dotted line, figure 14*d*).

Profiles of spatially averaged Reynolds shear stress $\langle R_{13}\rangle$, normalised by the square of the mean friction velocity, are plotted against wall-normal position for Groups A, B and C in figure 16, where smooth-wall data at matched flow conditions are included for comparison. Again, looking from left-to-right across figures 16(*a–c*), it is clear that the best collapse between the smooth- and rough-wall data is observed for Group C (blue lines), and the worst overall collapse is observed above surface 010_010 (dotted red line, figure 16*a*), which is in line with the behaviour of the corresponding streamwise Reynolds stress profile (red dotted line, figure 15*a*). One explanation for this behaviour is that the contribution of dispersive shear stress $\langle D_{13}\rangle$ to the total shear stress becomes increasingly large as ES_y decreases. Assuming that the viscous shear stress is negligible for heights greater than $x_3/h_{max} > 1$, the total shear stress varies linearly as $1 - x_3/\delta \approx -(\langle R_{13}\rangle + \langle D_{13}\rangle)$ above the roughness crests, which means that any increase in dispersive

shear stress must be met by a decrease in Reynolds shear stress (and vice versa). The sum of Reynolds and dispersive shear stress, $(\langle R_{13}\rangle + \langle D_{13}\rangle)$, normalised by the square of the mean friction velocity, is plotted against outer-scaled wall-normal position in figures 16(*d–f*). The data exhibit an almost perfect linear variation between the highest roughness crest ($x_3/h_{max} = 1$) and the channel half-height ($x_3/\delta = 1$), which, in addition to verifying that viscous stresses are indeed negligible in the outer region, also confirms that the present simulations have achieved satisfactory levels of statistical convergence; e.g. see Vinuesa *et al.* (2016) for details. Differences between the total shear stress (figures 16*d–f*) and spatially averaged Reynolds shear stress profiles (figures 16*a–c*) above the roughness crests therefore arise as a direct result of non-negligible dispersive shear stress, which increases above low-ES_x surfaces as ES_y is reduced.

To associate particular length scales to the levels of spatially averaged Reynolds shear stress (figure 16), the co-spectra of instantaneous $u_1'u_3'$ fluctuations can be examined. This allows analysis of the energetic contributions from different wavelengths, e.g. in the streamwise direction, $\langle R_{13}\rangle(x_3) = \int_0^\infty \Phi_{13}(\lambda_1, x_3)\,\mathrm{d}\log(\lambda_1)$, where $\Phi_{13}(\lambda_1, x_3) = \kappa_1\,\phi_{13}(\lambda_1, x_3)$ is the premultiplied co-spectrum of u_1' and u_3', and κ_1 is the streamwise wavenumber. Whilst the behaviour and scaling of Reynolds shear stress co-spectra in smooth-walled turbulent channel flow are well-documented (Del Alamo *et al.* 2004; Lee & Moser 2015), data are less common above irregular rough walls. Here, the spectral decomposition of Reynolds shear stress is compared for surfaces 010_010 and 010_035, and the reference smooth-wall data, with the aim of identifying the range of scales that exhibit the most (or least) sensitivity with respect to ES_y.

Contours of streamwise premultiplied Reynolds shear stress co-spectra normalised by the square of the mean friction velocity are plotted against inner-scaled wall-normal position for surfaces 010_035 and 010_010 in figures 17(*a*,*b*), respectively. Looking first at figure 17(*a*), it is clear that the co-spectra for surface 010_035 (blue lines) collapse on top of the smooth-wall data (grey lines) above wall-normal heights greater than $x_3^+ \gtrsim 100$. In addition, the peak energy in the streamwise premultiplied co-spectra occurs just above the roughness crests and is concentrated at wavelengths approximately equal to the mean streamwise roughness wavelength ($\bar{\lambda}_x/\delta \approx 1$, horizontal black line, figure 17*a*). Previous analyses of streamwise premultiplied energy spectra of streamwise velocity fluctuations in turbulent pipe flow above isotropic egg-carton roughness have shown similar behaviour at comparable flow conditions (Chan *et al.* 2018). Whilst the peak energy in the surface 010_010 co-spectra (red lines, figure 17*b*) also occurs just above the roughness crests and is concentrated at wavelengths approximately equal to the mean streamwise roughness wavelength, the data show a clear disagreement with the smooth-wall data above wall-normal heights greater than $x_3^+ \gtrsim 100$ and for streamwise wavelengths greater than $\lambda_x^+ \gtrsim 500$. This observation implies that the turbulence structure above surface 010_010 has undergone a broadband spectral change. To quantify these changes, the smooth-wall Reynolds shear stress co-spectrum was subtracted from its rough-wall counterpart using the formula $\Delta\Phi_{13}(\lambda_1, x_3) \equiv \kappa_1[\phi_{13,r}(\lambda_1, x_3) - \phi_{13,s}(\lambda_1, x_3)]$, where subscripts r and s denote rough- and smooth-wall data, respectively.

The difference between the smooth-wall and surface 010_035 Reynolds shear stress co-spectra is shown in figure 17(*c*), where solid and dotted lines denote an energy surplus ($\Delta\phi_{13} > 0$) and an energy defect ($\Delta\phi_{13} < 0$), respectively. As expected, negligible energetic differences ($\Delta\phi_{13} \approx 0$) are observed across all streamwise wavelengths above wall-normal heights greater than $x_3^+ \gtrsim 100$, since the smooth- and rough-wall co-spectra collapse in the same region (see figure 17*a*). Negligible energetic differences are also observed where the roughness-induced secondary motions become small, i.e. above

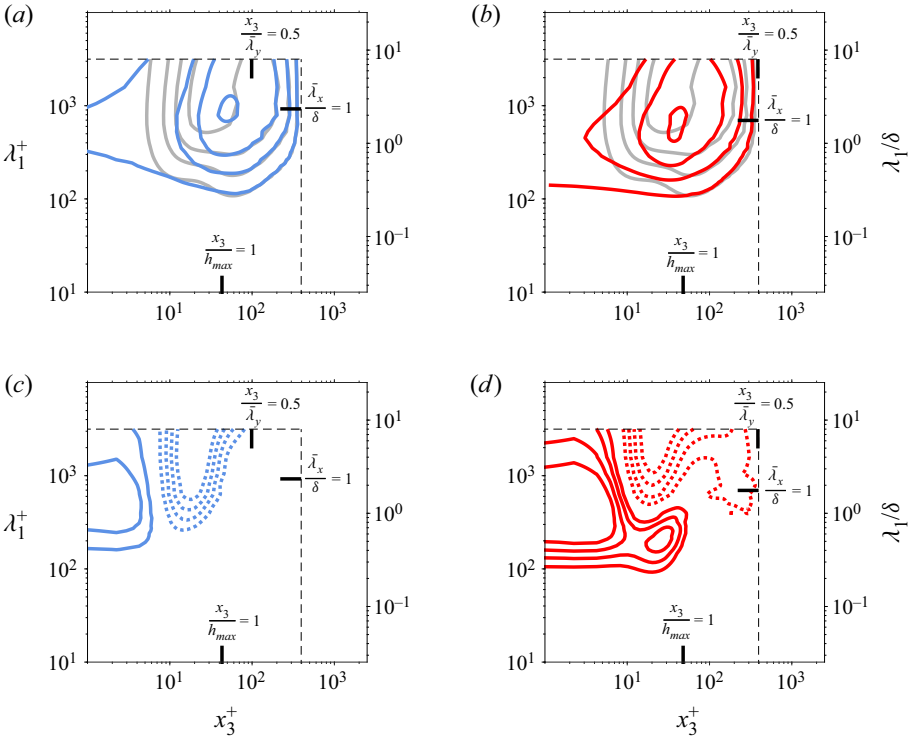

Figure 17. Comparison of streamwise premultiplied Reynolds shear stress co-spectra between the reference smooth wall (grey line) and (*a*) surface 010_035 (blue line), and (*b*) surface 010_010 (red line). The vertical black lines on the lower and upper horizontal axis denote the height of the highest roughness crest ($x_3/h_{max} = 1$) and the wall-normal extent of the dispersive stresses $x_3 = 0.5\bar{\lambda}_y$ proposed by Chan *et al.* (2018), respectively. The horizontal black line denotes the mean streamwise roughness wavelength ($\bar{\lambda}_x/\delta = 1$). Vertical and horizontal black dashed lines denote the wall-normal height of the channel half-height ($x_3/\delta = 1$) and the streamwise length of the computational domain (L_1/δ), respectively. Contour lines in (*a*,*b*) are shown on the levels $\{0.05, 0.13, 0.21, 0.29\}$. The differences between the smooth-wall co-spectra and rough-wall co-spectra for (*c*) surface 010_035 and (*d*) surface 010_010 are also shown, where dotted and solid lines denote an energetic deficit ($\Delta\phi_{13} < 0$) and surplus ($\Delta\phi_{13} > 0$), respectively. Positive and negative contour lines in (*c*,*d*) are shown on the levels $\{0.025, 0.043, 0.062, 0.080\}$ and $-\{0.025, 0.050, 0.075, 0.100\}$, respectively.

wall-normal heights greater than $x_3/\bar{\lambda}_y > 0.5$, as proposed by Chan *et al.* (2018) (see figure 12*b*). In contrast, an energy defect is evident in the vicinity of the highest roughness crests ($x_3/h_{max} = 1$) for streamwise wavelengths greater than $\lambda_x^+ \gtrsim 250$, with the strongest defect concentrated at wavelengths approximately equal to the mean streamwise roughness wavelength ($\bar{\lambda}_x/\delta \approx 1$). The net effect of these energy-deficient scales explains why the peak value of the spatially averaged Reynolds shear stress profile is suppressed above surface 010_035 (dotted blue line, figure 16*c*), relative to the smooth-wall value (grey line, figure 16*c*), and is consistent with the notion that surface roughness disrupts the near-wall turbulence cycle (Schultz & Flack 2007; Squire *et al.* 2016). In the vicinity of the mean roughness height, an energy surplus is evident for streamwise wavelengths greater than $\lambda_x^+ \gtrsim 180$, which explains why the levels of spatially averaged Reynolds shear stress around $x_3^+ \approx 0$ for surface 010_035 (dotted blue line, figure 16*c*) exceed smooth-wall levels (grey line, figure 16*c*).

The difference between the smooth-wall and surface 010_010 co-spectra is shown in figure 17(*d*). In contrast to the surface 010_035 data (figure 17*c*), the data above surface 010_010 reveal an energy defect that penetrates deep into the outer region for streamwise wavelengths of the order of the mean streamwise roughness wavelength, i.e. $\bar{\lambda}_x/\delta \approx 1.0$ (red dotted lines). The net effect of these energy-deficient scales explains why the Reynolds shear stress profile for surface 010_010 fails to collapse onto the smooth-wall data in the outer region (dotted red line, figure 16*a*) and why such poor levels of outer-layer similarity are observed. Further, the wall-normal extent of the energy defect above surface 010_010 is consistent with the height of the roughness sublayer inferred from the cross-stream distribution of streamwise dispersive velocity (figure 12*a*), as well as the dimensions of roughness-induced secondary motions identified using signed swirl strength (figure 13*d*).

Contours of spanwise premultiplied Reynolds shear stress co-spectra normalised by the square of the mean friction velocity are plotted against inner-scaled wall-normal position for surfaces 010_035 and 010_010 in figures 18(*a*,*b*), respectively. Overall, the spanwise co-spectra show similar trends to their streamwise counterparts (figures 17*a*,*b*). In particular, the spanwise co-spectra above surface 010_035 (figure 17*c*) show good levels of agreement with the smooth-wall data in the outer region, whereas the surface 010_010 data show obvious disagreement over a range of scales (figure 17*d*). The differences between the smooth-wall spanwise co-spectra and the data for surfaces 010_035 and 010_010 are shown in figures 18(*c*) and 18(*d*), respectively. Again, whilst negligible energetic differences are observed for wall normal heights greater than $x_3^+ \gtrsim 100$ above surface 010_035 (figure 18*c*), an energy defect extends deep into the outer region above surface 010_010 (figure 18*d*), which indicates that the turbulence structure, even far from the wall, is profoundly altered above the latter, lower-ES_y surface. As a result, whereas diminished levels of outer-layer similarity are observed above surface 010_010, the surface 010_035 co-spectra retain outer-layer similarity on a scale-by-scale basis.

4. Conclusions

Fully developed turbulent channel flow over irregular, three-dimensional rough walls with systematically varied values of spanwise effective slope (ES_y) was studied using direct numerical simulations (DNS) at friction Reynolds number 395, corresponding to viscous-scaled roughness height $k^+ \approx 65.8$ (where k is the mean peak-to-valley height). A set of ten near-Gaussian roughness topographies with specified values of ES_y, three separate values of streamwise effective slope ES_x, and common mean peak-to-valley height, were synthesised using a surface generation algorithm (figure 3). The instantaneous DNS data were reduced using the double-averaged (DA) methodology, and the sensitivity of DA statistics with respect to ES_y for each value of ES_x was studied for a fixed value of k^+ in the context of the Hama roughness function (figures 5 and 6), the fractional contribution of spatially averaged pressure drag to total drag (figures 7 and 8), mean velocity profiles (figures 9 and 11), dispersive streamwise velocity (figure 12), roughness-induced secondary motions (figure 13), dispersive normal stresses (figure 14), spatially averaged Reynolds shear stress (figure 16) and Reynolds shear stress co-spectra (figures 17 and 18). The contributions of this work are discussed below.

The key finding of this work is that ES_y emerges as a key topographical parameter as its streamwise counterpart ES_x becomes small. One interpretation of this behaviour is that ES_y becomes more important as the 'waviness' regime is approached, which, according to Schultz & Flack (2009), occurs for surfaces with $ES_x \lesssim 0.35$. In this regime, viscous drag can become non-negligible and the flow is considered to be transitionally rough.

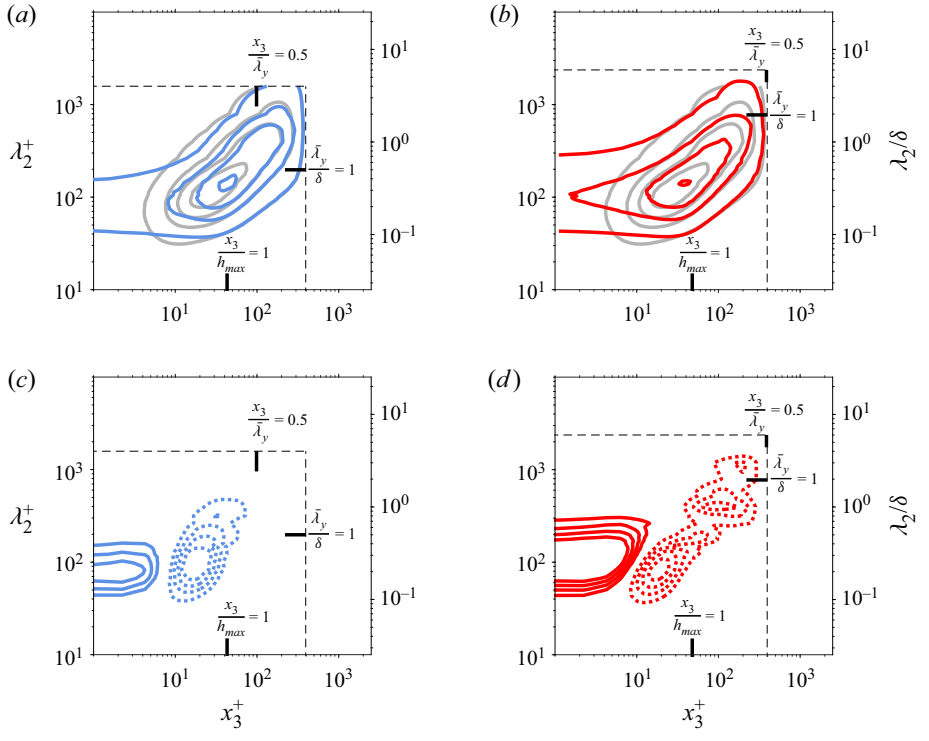

Figure 18. Comparison of spanwise premultiplied Reynolds shear stress co-spectra between the reference smooth wall (grey line) and (*a*) surface 010_035 (blue line), and (*b*) surface 010_010 (red, line). The vertical black lines on the lower and upper horizontal axis denote the height of the highest roughness crest ($x_3/h_{max} = 1$) and the wall-normal extent of the dispersive stresses $x_3 = 0.5\bar{\lambda}_y$ proposed by Chan *et al.* (2018), respectively. The horizontal black line denotes the mean streamwise roughness wavelength ($\bar{\lambda}_x/\delta = 1$). Vertical and horizontal black dashed lines denote the wall-normal height of the channel half-height ($x_3/\delta = 1$) and the spanwise width of the computational domain (L_2/δ), respectively. Contour lines in (*a*,*b*) are shown on the levels {0.05, 0.20, 0.35, 0.50}. The differences between the smooth-wall co-spectra and rough-wall co-spectra for (*c*) surface 010_035 and (*d*) surface 010_010 are also shown, where dotted and solid lines denote an energetic deficit ($\Delta\phi_{13} < 0$) and surplus ($\Delta\phi_{13} > 0$), respectively. Positive and negative contour lines in (*c*,*d*) are shown on the levels {0.050, 0.075, 0.100, 0.125} and $-${0.050, 0.083, 0.117, 0.150}, respectively.

For instance, Napoli *et al.* (2008) report that viscous and pressure drag are approximately equal on two-dimensional irregular sine wave roughness with $ES_x = 0.15$ at viscous-scaled mean absolute roughness height $k^+ \approx 14$. MacDonald *et al.* (2016) report that viscous drag dominates pressure drag on isotropic three-dimensional egg-carton roughness with $ES_x \lesssim 0.35$ at viscous-scaled sinusoidal semi-amplitude $k^+ = 10$. Under these conditions, spanwise variations in surface elevation, $\partial h/\partial x_2$, and hence variations in S_y, can affect directly the global force balance through the viscous term (3.1). However, it is worth noting that low-ES_x surfaces that fall within the wavy regime can also exhibit fully rough behaviour, where viscous drag is overwhelmed by pressure drag ($F_p \gg F_v$). For instance, Nugroho *et al.* (2021) report fully rough behaviour for their 'rough 2.5×' orange-peel surface ($ES_x = ES_x \approx 0.08$), where the Hama roughness function varies as $\Delta U^+_{FR}(k_s^+) = \kappa^{-1} \log Ck^+ + A - 8.5$ (where $C = k_s/k \approx 2.45$, and k is the mean absolute height). Under these flow conditions, it is possible that the Hama roughness function will exhibit limited sensitivity with respect to variations in ES_y, since its effect can no longer

be transmitted through the viscous term. However, the effect of varying ES_y under fully rough conditions was not investigated by Nugroho *et al.* (2021) since their work considered isotropic roughness ($ES_y/ES_x = 1$). Most of the data in the present study fall within the transitionally rough regime, and as a result, an appreciable sensitivity with respect to ES_y was retained – particularly for low-ES_x surfaces that have the highest proportion of viscous drag. Past work by Thakkar *et al.* (2016) and Jouybari *et al.* (2021) has also identified ES_y as an important topographical parameter at comparable flow conditions. The present study complements this past work by providing a detailed account of the physical mechanisms that determine the sensitivity of ΔU^+ with respect to systematic variations in ES_y for a fixed value of k^+.

A secondary finding of this work is that particular low-ES_y surfaces investigated here can cause a breakdown of outer-layer similarity in both mean flow and turbulence statistics (for a fixed value of k^+). Diminished levels of outer-layer similarity became most pronounced for the lowest value of ES_x and ES_y investigated here ($ES_x = ES_y = 0.1$). This behaviour was attributed to insufficient scale separation between the outer length scale δ and the in-plane spanwise roughness wavelength $\bar{\lambda}_y$. To be specific, as $\bar{\lambda}_y$ approaches δ, spanwise variations in time-averaged streamwise velocity were observed to extend up to (and beyond) the channel half-height δ. Similar observations have been made in the context of two-dimensional strip roughness (Yang & Anderson 2018), multi-scale cuboid roughness (Medjnoun *et al.* 2021) and three-dimensional egg-carton roughness (Chan *et al.* 2018) when $\bar{\lambda}_y$ becomes an appreciable proportion of the boundary layer thickness. Here, the mean-squared effect of these δ-scale motions led to non-negligible levels of dispersive stress in the outer region, which, as noted by Jelly & Busse (2018), play a direct role in determining the the local value of ΔU^+ above the roughness crests. An examination of Reynolds shear stress co-spectra also revealed diminished levels of outer-layer similarity above low-ES_y surfaces, implying that the turbulence structure, even far from the wall, is affected across a wide range of energy-containing scales. Overall, these observations add to the growing body of literature that the thickness of the roughness sublayer is a direct function of the spanwise in-plane roughness wavelength (Chan *et al.* 2018; Medjnoun *et al.* 2021) and that as this length scale becomes an appreciable fraction of the outer length scale, non-equilibrium behaviours emerge in both mean and turbulence statistics.

Supplementary material. Supplementary material is available at https://doi.org/10.1017/jfm.2022.823.

Funding. We gratefully acknowledge support by the United Kingdom Engineering and Physical Sciences Research Council via grant no. EP/P009875/1, and by the Australian Research Council. This work used the Cirrus UK National Tier-2 HPC Service at EPCC (http://www.cirrus.ac.uk) funded by the University of Edinburgh and EPSRC (EP/P020267/1). T.O.J. gratefully acknowledges the financial support of the University of Melbourne Early Career Researcher Award. A.B. gratefully acknowledges support via a Leverhulme Trust Research Fellowship.

Declaration of interests. The authors report no conflict of interest.

Data availability statement. Surface and velocity data are openly available from the University of Leicester research repository under https://doi.org/10.25392/leicester.data.21324765.

Author ORCIDs.
T.O. Jelly https://orcid.org/0000-0001-5314-7768;
A. Ramani https://orcid.org/0000-0002-0782-6441;
B. Nugroho https://orcid.org/0000-0002-2033-7052;
N. Hutchins https://orcid.org/0000-0003-1599-002X;
A. Busse https://orcid.org/0000-0002-3496-6036.

Appendix A. Numerical details of the surface synthesis procedure

Irregular surface roughness with specified statistical properties was generated using the multi-scale anisotropic rough surface (MARS) algorithm (Jelly & Busse 2018, 2019*a*). Doubly periodic height maps h_{ij} were synthesised by taking linear combinations of Gaussian random number matrices using a weighted moving average (MA) process, which can be expressed as

$$h_{ij} = \sum_{k=1}^{n_1} \sum_{l=1}^{n_2} \alpha_{kl}\, \eta_{rs}, \quad \begin{cases} i = 1, 2, \ldots, N_1, \\ j = 1, 2, \ldots, N_2, \\ r = [i + k - 1 \pmod{N_1})] + 1, \\ s = \big[j + l - 1 \pmod{N_2}\big] + 1, \end{cases} \tag{A1}$$

where η_{ij} is an $N_1 \times N_2$ matrix of uncorrelated Gaussian random numbers, the α_{kl} are an $n_1 \times n_2$ set of coefficients, and mod denotes the modulo operator.

In (A1), the MA coefficients α_{kl} were determined by solving the system of nonlinear equations

$$R_{pq} = \sum_{k=1}^{n_1 - p} \sum_{l=1}^{n_2 - q} \alpha_{kl}\, \alpha_{k+p, l+q}, \quad \begin{cases} p = 0, 1, \ldots, n_1 - 1, \\ q = 0, 1, \ldots, n_2 - 1, \end{cases} \tag{A2}$$

using an iterative Newton-based method outlined in past work by Patir (1978), where R_{pq} is the discrete autocorrelation function (ACF).

Each height map was generated with a specified exponential ACF

$$R(\Delta x_1, \Delta x_2) = \exp\left(-2.3\sqrt{\left(\frac{\Delta x_1}{\Delta x_1^*}\right)^2 + \left(\frac{\Delta x_2}{\Delta x_2^*}\right)^2}\right), \tag{A3}$$

where Δx_1, Δx_2 denote the spatial separations in the streamwise and spanwise directions, respectively, and Δx_1^*, Δx_2^* denote the spatial separations at which the streamwise and spanwise ACF profiles reduce to 10 % of their values at the origin.

To generate each surface shown in figure 3, the values of Δx_1 and Δx_2 were varied systematically to generate a set of MA coefficients that yielded the desired combination of ES_x and ES_y.

Appendix B. Derivation of global hydrodynamic force balance

Following Peet & Sagaut (2009), the streamwise component of the local, time-averaged hydrodynamic force per unit area that acts on a surface can be expressed as

$$\overline{F}_1(\boldsymbol{x}) = -\left[\mu\left(\frac{\partial \bar{u}_1}{\partial x_j} + \frac{\partial \bar{u}_j}{\partial x_1}\right)\hat{n}_j - \bar{p}_s \hat{n}_1\right], \tag{B1}$$

where $\hat{n}_j = \nabla h / \|\nabla h\|$ is the unit normal vector of the height map, and $\bar{p}_s$ is the local surface pressure.

After integrating (B1) with respect to the incremental surface area dS, the mean viscous force per unit area acting on the surface can be written as

$$\langle F_v \rangle = \iint_S -\mu \left[2\,\frac{\partial \bar{u}_1}{\partial x_1}\,\frac{\partial h}{\partial x_1} + \left(\frac{\partial \bar{u}_1}{\partial x_2} + \frac{\partial \bar{u}_2}{\partial x_1} \right) \frac{\partial h}{\partial x_2} - \left(\frac{\partial \bar{u}_1}{\partial x_3} + \frac{\partial \bar{u}_3}{\partial x_1} \right) \right] \frac{1}{\|\boldsymbol{\nabla} h\|}\,\mathrm{d}S, \quad \text{(B2)}$$

and the mean pressure force per unit area acting on the surface can be written as

$$\langle F_p \rangle = \iint_S \left[(\bar{p}_s - \bar{p}_0)\,\frac{\partial h}{\partial x_1} \right] \frac{1}{\|\boldsymbol{\nabla} h\|}\,\mathrm{d}S, \quad \text{(B3)}$$

where p_s has been referenced relative to an arbitrary gauge pressure, taken here as the mean surface pressure, i.e. $\bar{p}_0 \equiv A^{-1} \iint \bar{p}_s(x_1, x_2)\,\mathrm{d}A$.

For streamwise homogeneous surface roughness with $\partial h/\partial x_1 = 0$ and a streamwise homogeneous time-averaged velocity field $\partial \bar{u}_i/\partial x_1 = 0$, the hydrodynamic force balance reduces to

$$\langle F_1 \rangle = \iint_S -\mu \left[\frac{\partial \bar{u}_1}{\partial x_2}\,\frac{\partial h}{\partial x_2} - \frac{\partial \bar{u}_1}{\partial x_3} \right] \frac{1}{\|\boldsymbol{\nabla} h\|}\,\mathrm{d}S. \quad \text{(B4)}$$

For spanwise homogeneous surface roughness with $\partial h/\partial x_2 = 0$ and a spanwise homogeneous time-averaged velocity field $\partial \bar{u}_i/\partial x_2 = 0$, the hydrodynamic force balance reduces to

$$\langle F_1 \rangle = \iint_S \left(-\mu \left[2\,\frac{\partial \bar{u}_1}{\partial x_1}\,\frac{\partial h}{\partial x_1} - \left(\frac{\partial \bar{u}_1}{\partial x_3} + \frac{\partial \bar{u}_3}{\partial x_1} \right) \right] \frac{1}{\|\boldsymbol{\nabla} h\|} + \left[(\bar{p}_s - \bar{p}_0)\,\frac{\partial h}{\partial x_1} \right] \frac{1}{\|\boldsymbol{\nabla} h\|} \right) \mathrm{d}S. \quad \text{(B5)}$$

References

Adrian, R.J., Christensen, K.T. & Liu, Z.-C. 2000 Analysis and interpretation of instantaneous turbulent velocity fields. *Exp. Fluids* **29** (3), 275–290.

Allen, J.J., Shockling, M.A., Kunkel, G.J. & Smits, A.J. 2007 Turbulent flow in smooth and rough pipes. *Phil. Trans. R. Soc.* A **365** (1852), 699–714.

Bakhuis, D., Ezeta, R., Berghout, P., Bullee, P.A, Tai, D., Chung, D., Verzicco, R., Lohse, D., Huisman, S.G. & Sun, C. 2020 Controlling secondary flow in Taylor–Couette turbulence through spanwise-varying roughness. *J. Fluid. Mech.* **883**, A15.

Barros, J.M. & Christensen, K.T. 2014 Observations of turbulent secondary flows in a rough-wall boundary layer. *J. Fluid Mech.* **748**, R1.

Berghout, P., Bullee, P.A., Fuchs, T., Scharnowski, S., Kähler, C.J., Chung, D., Lohse, D. & Huisman, S.G. 2021 Characterizing the turbulent drag properties of rough surfaces with a Taylor–Couette set-up. *J. Fluid Mech.* **919**, A7.

Bhaganagar, K., Kim, J. & Coleman, G. 2004 Effect of roughness on wall-bounded turbulence. *Flow Turbul. Combust.* **72** (2–4), 463–492.

Bons, J. 2005 A critical assessment of Reynolds analogy for turbine flows. *Trans. ASME J. Heat Transfer* **127** (5), 472–485.

Brunet, Y. 2020 Turbulent flow in plant canopies: historical perspective and overview. *Boundary-Layer Meteorol.* **177** (2), 315–364.

Busse, A. & Jelly, T.O. 2020 Influence of surface anisotropy on turbulent flow over irregular roughness. *Flow Turbul. Combust.* **104**, 331–354.

Busse, A., Lützner, M. & Sandham, N.D. 2015 Direct numerical simulation of turbulent flow over a rough surface based on a surface scan. *Comput. Fluids* **116**, 129–147.

Busse, A., Thakkar, M. & Sandham, N.D. 2017 Reynolds-number dependence of the near-wall flow over irregular rough surfaces. *J. Fluid Mech.* **810**, 196–224.

Castro, I. 2007 Rough-wall boundary layers: mean flow universality. *J. Fluid Mech.* **585**, 469–485.

Chan, L., MacDonald, M., Chung, D., Hutchins, N. & Ooi, A. 2015 A systematic investigation of roughness height and wavelength in turbulent pipe flow in the transitionally rough regime. *J. Fluid Mech.* **771**, 743–777.

CHAN, L., MACDONALD, M., CHUNG, D., HUTCHINS, N. & OOI, A. 2018 Secondary motion in turbulent pipe flow with three-dimensional roughness. *J. Fluid Mech.* **854**, 5–33.

CHUNG, D., CHAN, L., MACDONALD, M., HUTCHINS, N. & OOI, A. 2015 A fast direct numerical simulation method for characterising hydraulic roughness. *J. Fluid Mech.* **773**, 418–431.

CHUNG, D., MONTY, J.P. & HUTCHINS, N. 2018 Similarity and structure of wall turbulence with lateral wall shear stress variations. *J. Fluid Mech.* **847**, 591–613.

CHUNG, D.C., HUTCHINS, N., SCHULTZ, M.P. & FLACK, K.A. 2021 Predicting the drag of rough surfaces. *Annu. Rev. Fluid Mech.* **53**, 439–471.

COCEAL, O., THOMAS, T.G., CASTRO, I.P. & BELCHER, S.E. 2006 Mean flow and turbulence statistics over groups of urban-like cubical obstacles. *Boundary-Layer Meteorol.* **121** (3), 491–519.

DE MARCHIS, M., SACCONE, D., MILICI, B. & NAPOLI, E. 2020 Large eddy simulations of rough turbulent channel flows bounded by irregular roughness: advances toward a universal roughness correlation. *Flow Turbul. Combust.* **105**, 627–648.

DEL ALAMO, J.C., JIMÉNEZ, J., ZANDONADE, P. & MOSER, R.D. 2004 Scaling of the energy spectra of turbulent channels. *J. Fluid Mech.* **500**, 135–144.

FLACK, K.A. 2018 Moving beyond Moody. *J. Fluid Mech.* **842**, 1–4.

FLACK, K.A., SCHULTZ, M.P. & SHAPIRO, T.A. 2005 Experimental support for Townsend's Reynolds number similarity hypothesis on rough walls. *Phys. Fluids.* **17** (3), 035102.

FLACK, K.A., SCHULTZ, M.P. & BARROS, J.M. 2020 Skin friction measurements of systematically-varied roughness: probing the role of roughness amplitude and skewness. *Flow Turbul. Combust.* **104** (2), 317–329.

FLACK, K.A., SCHULTZ, M.P., BARROS, J.M. & KIM, Y.C. 2016 Skin-friction behavior in the transitionally-rough regime. *Intl J. Heat Fluid Flow* **61**, 21–30.

FOROOGHI, P., STRIPF, M. & FROHNAPFEL, B. 2018*a* A systematic study of turbulent heat transfer over rough walls. *Intl J. Heat Mass Transfer* **127**, 1157–1168.

FOROOGHI, P., STROH, A., MAGAGNATO, F., JAKIRLIC, S. & FROHNAPFEL, B. 2017 Towards a universal roughness correlation. *ASME J. Fluids Engng* **139** (12), 12121.

FOROOGHI, P., STROH, A., SCHLATTER, P. & FROHNAPFEL, B. 2018*b* Direct numerical simulation of flow over dissimilar, randomly distributed roughness elements: a systematic study on the effect of surface morphology on turbulence. *Phys. Rev. Fluids* **3** (4), 044605.

GATTI, D., VON DEYN, L., FOROOGHI, P. & FROHNAPFEL, B. 2020 Do riblets exhibit fully rough behaviour? *Exp. Fluids* **61** (3), 81.

GEORGE, W.K. 2007 Is there a universal log law for turbulent wall-bounded flows? *Phil. Trans. R. Soc.* A **365** (1852), 789–806.

GRAY, W.G. & LEE, P.C.Y. 1977 On the theorems for local volume averaging of multiphase systems. *Intl J. Multiphase Flow* **3** (4), 333–340.

HAMA, F.R. 1954 Boundary layer characteristics for smooth and rough surfaces. *Trans. Soc. Nav. Archit. Mar. Engrs* **62**, 333–358.

JELLY, T.O. & BUSSE, A. 2018 Reynolds and dispersive shear stress contributions above highly skewed roughness. *J. Fluid Mech.* **852**, 710–724.

JELLY, T.O. & BUSSE, A. 2019*a* Multi-scale anisotropic rough surface algorithm: technical documentation and user guide. *Tech. Rep.* University of Glasgow.

JELLY, T.O. & BUSSE, A. 2019*b* Reynolds number dependence of Reynolds and dispersive stresses in turbulent channel flow past irregular near-Gaussian roughness. *Intl J. Heat Fluid Flow* **80**, 108485.

JIMÉNEZ, J. 2004 Turbulent flows over rough walls. *Annu. Rev. Fluid Mech.* **36**, 173–196.

JOUYBARI, M.A., YUAN, J., BRERETON, G.J. & MURILLO, M.S. 2021 Data-driven prediction of the equivalent sand-grain height in rough-wall turbulent flows. *J. Fluid Mech.* **912**, A8.

KROGSTAD, P.Å. & EFROS, V. 2012 About turbulence statistics in the outer part of a boundary layer developing over two-dimensional surface roughness. *Phys. Fluids* **24** (7), 075112.

LEE, M. & MOSER, R.D. 2015 Direct numerical simulation of turbulent channel flow up to $Re_\tau \approx 5200$. *J. Fluid Mech.* **774**, 395–415.

MA, G.-Z., XU, C.-X., SUNG, H.J. & HUANG, W.-X. 2020 Scaling of rough-wall turbulence by the roughness height and steepness. *J. Fluid Mech.* **900**, R7.

MA, R., ALAMÉ, K. & MAHESH, K. 2021 Direct numerical simulation of turbulent channel flow over random rough surfaces. *J. Fluid Mech.* **908**, A40.

MACDONALD, M., CHAN, L., CHUNG, D., HUTCHINS, N. & OOI, A. 2016 Turbulent flow over transitionally rough surfaces with varying roughness densities. *J. Fluid Mech.* **804**, 130–161.

MacDonald, M., Hutchins, N. & Chung, D. 2019 Roughness effects in turbulent forced convection. *J. Fluid Mech.* **861**, 138–162.

Medjnoun, T., Rodriguez-Lopez, E., Ferreira, M.A., Griffiths, T., Meyers, J. & Ganapathisubramani, B. 2021 Turbulent boundary-layer flow over regular multiscale roughness. *J. Fluid Mech.* **917**, A1.

Meyers, J., Ganapathisubramani, B. & Cal, R.B. 2019 On the decay of dispersive motions in the outer region of rough-wall boundary layers. *J. Fluid Mech.* **862**, R5.

Modesti, D., Endrikat, S., Hutchins, N. & Chung, D. 2021 Dispersive stresses in turbulent flow over riblets. *J. Fluid Mech.* **917**, A55.

Moltchanov, S., Bohbot-Raviv, Y. & Shavit, U. 2011 Dispersive stresses at the canopy upstream edge. *Boundary-Layer Meteorol.* **139** (2), 333–351.

Monty, J.P., Dogan, E., Hanson, R., Scardino, A.J., Ganapathisubramani, B. & Hutchins, N. 2016 An assessment of the ship drag penalty arising from light calcareous tubeworm fouling. *Biofouling* **32** (4), 451–464.

Moody, L.F. 1944 Friction factors for pipe flow. *Trans. ASME* **66**, 671–684.

Napoli, E., Armenio, V. & De Marchis, M. 2008 The effect of the slope of irregularly distributed roughness elements on turbulent wall-bounded flows. *J. Fluid Mech.* **613**, 385–394.

Nikora, V., McEwan, I., McLean, S., Coleman, S., Pokrajac, D. & Walters, R. 2007 Double-averaging concept for rough-bed open-channel and overland flows: theoretical background. *J. Hydraul. Engng* **133** (8), 873–883.

Nikuradse, J. 1933 Strömungsgesetze in rauhen Rohren. *VDI-Forschungsheft* **361**.

Nugroho, B, Hutchins, N & Monty, J.P. 2013 Large-scale spanwise periodicity in a turbulent boundary layer induced by highly ordered and directional surface roughness. *Intl J. Heat Fluid Flow* **41**, 90–102.

Nugroho, B., Monty, J.P., Utama, I.K.A.P., Ganapathisubramani, B. & Hutchins, N. 2021 Non *k*-type behaviour of roughness when in-plane wavelength approaches the boundary layer thickness. *J. Fluid Mech.* **911**, A1.

Patir, N. 1978 A numerical procedure for random generation of rough surfaces. *Wear* **47** (2), 263–277.

Peet, Y. & Sagaut, P. 2009 Theoretical prediction of turbulent skin friction on geometrically complex surfaces. *Phys. Fluids* **21** (10), 105105.

Peeters, J.W.R. & Sandham, N.D. 2019 Turbulent heat transfer in channels with irregular roughness. *Intl J. Heat Mass Transfer* **138**, 454–467.

Pokrajac, D., McEwan, I. & Nikora, V. 2008 Spatially averaged turbulent stress and its partitioning. *Exp. Fluids* **45** (1), 73–83.

Portela, F.A., Busse, A. & Sandham, N.D. 2021 Numerical study of Fourier-filtered rough surfaces. *Phys. Rev. Fluids* **6** (8), 084606.

Raupach, M.R. & Shaw, R.H. 1982 Averaging procedures for flow within vegetation canopies. *Boundary-Layer Meteorol.* **22** (1), 79–90.

Scaggs, W.F., Taylor, R.P. & Coleman, H.W. 1988 Measurement and prediction of rough wall effects on friction factor – uniform roughness results. *Trans. ASME: J. Fluids Engng* **110**, 385–391.

Schultz, M.P. & Flack, K.A. 2007 The rough-wall turbulent boundary layer from the hydraulically smooth to the fully rough regime. *J. Fluid Mech.* **580**, 381–405.

Schultz, M.P. & Flack, K.A. 2009 Turbulent boundary layers on a systematically varied rough wall. *Phys. Fluids* **21** (1), 015104.

Seddighi, M., He, S., Pokrajac, D., O'Donoghue, T. & Vardy, A.E. 2015 Turbulence in a transient channel flow with a wall of pyramid roughness. *J. Fluid Mech.* **781**, 226–260.

Squire, D.T., Morrill-Winter, C., Hutchins, N., Schultz, M.P., Klewicki, J.C. & Marusic, I. 2016 Comparison of turbulent boundary layers over smooth and rough surfaces up to high Reynolds numbers. *J. Fluid Mech.* **795**, 210–240.

Thakkar, M., Busse, A. & Sandham, N.D. 2016 Surface correlations of hydrodynamic drag for transitionally rough engineering surfaces. *J. Turbul.* **18** (2), 138–169.

Thakkar, M., Busse, A. & Sandham, N.D. 2018 Direct numerical simulation of turbulent channel flow over a surrogate for Nikuradse-type roughness. *J. Fluid Mech.* **837**, R1.

Townsend, A., Senin, N., Blunt, L., Leach, R.K. & Taylor, J.S. 2016 Surface texture metrology for metal additive manufacturing: a review. *Precis. Engng* **46**, 34–47.

Townsend, A.A. 1976 *The Structure of Turbulent Shear Flow*, 2nd edn. Cambridge University Press.

Townsin, R.L. 1991 The correlation of added drag with surface roughness parameters. In *Recent Developments in Turbulence Management* (ed. K.S. Choi), pp. 181–191. Springer.

Townsin, R.L. 2003 The ship hull fouling penalty. *Biofouling* **19** (S1), 9–15.

UTAMA, I.K.A.P., NUGROHO, B., YUSUF, M., PRASETYO, F.A., HAKIM, M.L., SUASTIKA, I.K., GANAPATHISUBRAMANI, B., HUTCHINS, N. & MONTY, J.P. 2021 The effect of cleaning and repainting on the ship drag penalty. *Biofouling* **37** (4), 372–386.

VAN RIJ, J.A., BELNAP, B.J. & LIGRANI, P.M. 2002 Analysis and experiments on three-dimensional, irregular surface roughness. *J. Fluids Engng* **124** (3), 671–677.

VINUESA, R., PRUS, C., SCHLATTER, P. & NAGIB, H.M. 2016 Convergence of numerical simulations of turbulent wall-bounded flows and mean cross-flow structure of rectangular ducts. *Meccanica* **51** (12), 3025–3042.

VOLINO, R.J., SCHULTZ, M.P. & FLACK, K.A. 2009 Turbulence structure in a boundary layer with two-dimensional roughness. *J. Fluid Mech.* **635**, 75–101.

VOLINO, R.J., SCHULTZ, M.P. & FLACK, K.A. 2011 Turbulence structure in boundary layers over periodic two- and three-dimensional roughness. *J. Fluid Mech.* **676**, 172–190.

WANGSAWIJAYA, D.D., BAIDYA, R., CHUNG, D.C., MARUSIC, I. & HUTCHINS, N. 2020 The effect of spanwise wavelength of surface heterogeneity on turbulent secondary flows. *J. Fluid Mech.* **894**, A7.

YANG, J. & ANDERSON, W. 2018 Numerical study of turbulent channel flow over surfaces with variable spanwise heterogeneities: topographically-driven secondary flows affect outer-layer similarity of turbulent length scales. *Flow Turbul. Combust.* **100** (1), 1–17.

YANG, J. & BALARAS, E. 2006 An embedded-boundary formulation for large-eddy simulation of turbulent flows interacting with moving boundaries. *J. Comput. Phys.* **215** (1), 12–40.

YUAN, J. & PIOMELLI, U. 2014 Estimation and prediction of the roughness function on realistic surfaces. *J. Turbul.* **15** (6), 350–365.